Interfacial instability of confined three-dimensional active droplets

Bennett C. Sessa,[1,*] Federico Cao,[2,3,*] Robert A. Pelcovits,[4,5] Thomas R. Powers,[2,3,4,5] and Guillaume Duclos[1,†]

[1]*Department of Physics, Brandeis University, Waltham, Massachusetts 02453, USA*
[2]*School of Engineering, Brown University, Providence, Rhode Island 02912, USA*
[3]*Center for Fluid Mechanics, Brown University, Providence, Rhode Island 02912, USA*
[4]*Department of Physics, Brown University, Providence, Rhode Island 02912, USA*
[5]*Brown Theoretical Physics Center, Brown University, Providence, Rhode Island 02912, USA*

(Received 24 June 2025; revised 17 October 2025; accepted 19 December 2025; published 2 February 2026)

Instabilities of fluid-fluid interfaces occur in many forms within passive soft matter. Adding activity to one of the fluids can dramatically change the stability of the interface. Triggering active flows externally offers a unique opportunity to study the linear growth of the instability and quantitatively compare experiment and theory. We investigate the interfacial instability of a deformable three-dimensional active nematic liquid crystal droplet confined between two parallel plates. Spontaneous active flows drive the growth of undulations along the active/passive interface, with the mode number of the fastest-growing mode increasing with droplet radius and decreasing with gap height. Applying the lubrication approximation to a minimal nematohydrodynamic model reveals that the growth rates of the interfacial modes are determined by the active timescale and the relaxation timescales associated with liquid crystalline order as well as capillary and viscous stresses. We find multiple points of agreement between experiment and theory, including the shape evolution of individual droplets, the growth rates of unstable modes averaged across many droplets, and the extensional shear flows observed within droplets.

DOI: 10.1103/ytwv-7swk

Interfacial instabilities between immiscible fluids are ubiquitous across scales in nature, arising in systems ranging from geophysical flows [1,2] and industrial processes involving soft materials—such as additive manufacturing [3,4] and oil recovery [5,6]—to biological systems, including membraneless organelles [7], cells [8], tissues [9–12], suspensions of swimming organisms [13–17], and biofilms [18–20]. Such instabilities typically consist of a linear regime followed by a nonlinear regime, which may be chaotic. Studying the linear regime offers critical insight into the onset of the nonlinear regime and pattern formation [21]. In particular, the conditions for stability are often revealed theoretically through linear analysis. However, the linear regime is typically difficult to access experimentally because the time at which the instability begins must be carefully controlled. This is true for both passive fluids and active fluids composed of energy-consuming constituents [22–27]. To overcome this obstacle, we use phase-separated active fluids whose spontaneous flows, which displace the interface with the passive phase [28,29], can be triggered externally with light [30–33]. The combination of liquid-liquid phase separation and light-activable cytoskeletal proteins offers a unique opportunity to study the linear growth of interfacial deformations, revealing a regime difficult to access experimentally with uncontrolled active fluids [28,29,34,35].

Previous theoretical work elucidates the antagonistic roles that active and capillary forces play on the stability of active interfaces [36–41]. Below a critical activity, surface tension stabilizes all perturbations. Above this activity, a finite wavelength perturbation grows, and the fastest-growing mode increases with activity and droplet size [37,38,42]. However, most theoretical studies on activity-driven instabilities are in two dimensions (2D), while experiments with active fluids are often done in a three-dimensional (3D) geometry where the fluid is confined between two narrowly separated parallel plates [26,43], a configuration known as a Hele-Shaw cell [44]. Consequently, there is a need for a 3D theory that accounts for the dependence of the emergent dynamics on the separation between the plates. When the separation is thin compared to the characteristic in-plane length scale, lubrication theory is a well-established approximation that leads to a tractable model that still goes beyond the purely 2D theory.

In this paper, we combine experiments and theory to investigate the interfacial instability of 3D active droplets in a passive viscous fluid confined in a Hele-Shaw cell [Figs. 1(a) and 1(b)]. The active fluid is a 3D extensile active nematic liquid crystal in the isotropic phase. We apply a lubrication approximation to a minimal nematohydrodynamic model and find that the balance of active and restoring forces determines the most unstable mode. Active hydrodynamic flows

*These authors contributed equally to this work.
†Contact author: gduclos@brandeis.edu

Published by the American Physical Society under the terms of the Creative Commons Attribution 4.0 International license. Further distribution of this work must maintain attribution to the author(s) and the published article's title, journal citation, and DOI.

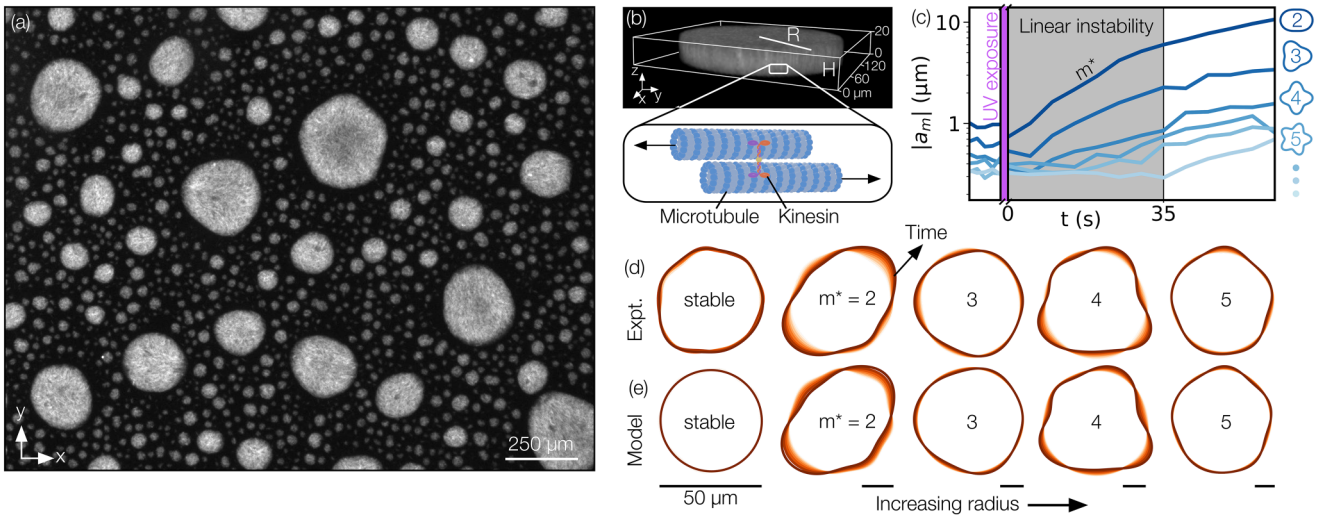


FIG. 1. Interfacial instability of active droplets confined in a Hele-Shaw cell. (a) Top view in the midplane of experimental active droplets (microtubules are fluorescent). (b) Confocal image of a confined, 3D active droplet containing extensile microtubule bundles and molecular motors. (c) Log-linear plot of time evolution of the radial mode amplitudes a_m. We shine UV light to uncage the ATP. (d) Time evolution of droplet interfaces experimentally and (e) theoretically after fitting the model parameters and retaining the first eight radial modes. Experimental and theoretical droplets have the same number of undulations with similar orientations. Color shows the time evolution from orange to red. Scale bars are all 50 μm, and droplet radius increases from left to right. Gap height $H = 20$ μm.

deform the low surface tension interface and equally excite all the radial interfacial modes. The passive restoring forces from surface tension and viscosity stabilize the interface. Due to the thin gap geometry, changing the droplet radius and gap height have opposite effects on the instability. Increasing droplet radius reduces the Laplace pressure, favoring the growth of high mode number (short wavelength) undulations. In contrast, increasing the gap height reduces viscous forces, favoring the growth of low mode number (long wavelength) undulations.

I. EXPERIMENTS

We study a 3D isotropic active liquid crystal composed of microtubules and adenosine triphosphate (ATP)-powered kinesin molecular motors [26,43,45] [Fig. 1(b)] embedded within a phase-separated polymeric fluid of polyethylene glycol (PEG) and Dextran [28]. The microtubules and the motors form extensile bundles that partition within the Dextran-rich phase, forming active droplets of various sizes surrounded by a passive PEG-rich viscous fluid [Fig. 1(a)]. The binary fluid is confined between two parallel plates that have been treated with a PEG brush to prevent wetting of the Dextran-rich active droplets [Fig. 1(b)]. Uncaging ATP with UV light triggers a transition from passive quiescent droplets to active droplets (Movie S1 in the Supplemental Material [46]). The extensile bundles form a continuously reconfiguring network that advects the surrounding fluid, powering spontaneous collective flows. It is important to note several features that differentiate these 3D active droplets from the well-established active nematic shells where kinesin-microtubule bundles are depleted at a 2D oil/water interface [26,35,47,48]. First, in our experiments, the extensile bundles are dispersed in 3D, completely filling the droplet, which was confirmed using 3D confocal microscopy [Fig. 1(b)]. Second, the microtubule bundles are dilute (∼0.1% volume fraction) forming a 3D active nematic liquid crystal in the isotropic phase [43,45], while the active shells are a dense 2D active nematic. Finally, the surface tension of the PEG/Dextran interface is almost six orders of magnitude lower than that of the oil/water interface, which allows for the interface to be deformed by the weak active flows [28].

We observe that after activation of the molecular motors, many small droplets do not change shape, whereas larger droplets systematically do, a phenomenon reminiscent of a morphological interfacial instability. In what follows, we focus on confined active droplets whose lateral dimensions exceed their height. As the droplet size increases, the number of ripples on the interface increases [Fig. 1(d)], in agreement with a hydrodynamic model presented below [Fig. 1(e)]. We decompose the interface into radial modes and find that the amplitude of the modes grows exponentially, with the fastest-growing mode corresponding to the number of ripples observed [Fig. 1(c)]. We did not observe any significant deformations along the z-axis [Fig. 1(b) and Movie S2 in the Supplemental Material [46]]. The exponential growth is followed by a nonlinear regime during which the active fluid continues to flow and the interfacial ripples chaotically grow, decay, and travel along the interface for hours until the ATP is fully consumed [28].

To be more quantitative, we measure the growth rates of the first ten modes of the interface for hundreds of droplets of varying radii and fixed thickness. We note that for a given droplet radius, the growth rates of the second harmonic are widely distributed with some positive and some negative, corresponding to unstable and stable droplets, respectively. For the smallest experimentally accessible radii, we observe a mixture of stable and unstable droplets. We cannot statis-

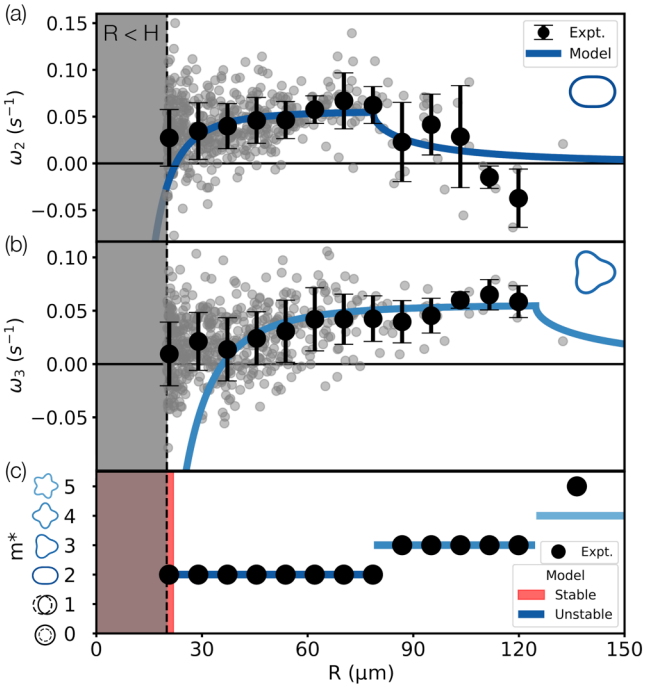


FIG. 2. Fastest-growing mode number increases with droplet radius for $H = 20\,\mu$m. Measured growth rates (disks) and model growth rates (lines) for the (a) second and (b) third radial modes. The model parameters are determined by fitting only ω_2. For ω_3, the model prediction is obtained without adjusting these parameters. Error bars represent the standard deviation of the binned growth rates. (c) Fastest-growing mode number m^* increases with droplet radius R.

tically measure a critical radius below which experimentally accessible droplets are stable. Still, we observe that the proportion of stable droplets decreases as their radius increases (Fig. 17). Binning similarly sized droplets together reveals that ω_2, the average growth rate of the second radial harmonic, initially increases and then decreases with droplet radius [Fig. 2(a)]. The average growth rate of the third radial harmonic, ω_3, also increases with radius [Fig. 2(b)] and becomes larger than ω_2 for $R \gtrsim 80\,\mu$m [Fig. 2(c)]. The widest droplets achievable experimentally exhibit growth of the fourth and fifth radial modes [Figs. 1(d), 2(c), and 16].We find that increasing the thickness of the confined droplet has the opposite effect as increasing the droplet radius. We measure the growth rates of the radial modes for droplets of varying radii and three different gap heights ranging from 20 to 100 μm. The droplet radius necessary to achieve a given growth rate must increase with increasing droplet thickness [Fig. 3(a)]. At a fixed radius, the fastest-growing mode number decreases with gap height [Fig. 3(b)]. In summary, thin and wide droplets ($R \gg H$) have higher fastest-growing mode numbers compared to thick and narrow droplets ($R \sim H$) that have lower fastest-growing mode numbers and tend to be stable.

II. MODEL

To understand our experimental observations, we develop a minimal hydrodynamic model. The experiments occur at low Reynolds number because of the small spatial dimensions and slow flows (Re $\sim 10^{-8}$, droplet size $\sim$100 μm, flow speed $\sim$1 μm/s, and viscosity $\sim$10 mPa s). The passive outer fluid is described by the Stokes equations. The active interior fluid is described by the Stokes equations with an additional active-stress term proportional to the divergence of the order parameter tensor Q, representing microtubule bundles modeled as active force dipoles [49]. The order parameter tensor Q evolves according to a nematohydrodynamic model for an incompressible extensile active nematic liquid crystal in the isotropic phase [50]. The equations are linearized about a state of no flow and isotropic phase, which corresponds to the state of the experimental droplets before the activity is turned on. Although the state is isotropic, liquid crystalline order emerges due to activity-driven shear flows; see Eq. (2) and Refs. [43,50,51]. A distinguishing feature of this work is the application of the lubrication approximation [52] to account for the fact that the droplets are wide and thin [Fig. 1(b)]. In this approximation, gradients in the velocity and the order parameter tensor across the gap are greater than gradients

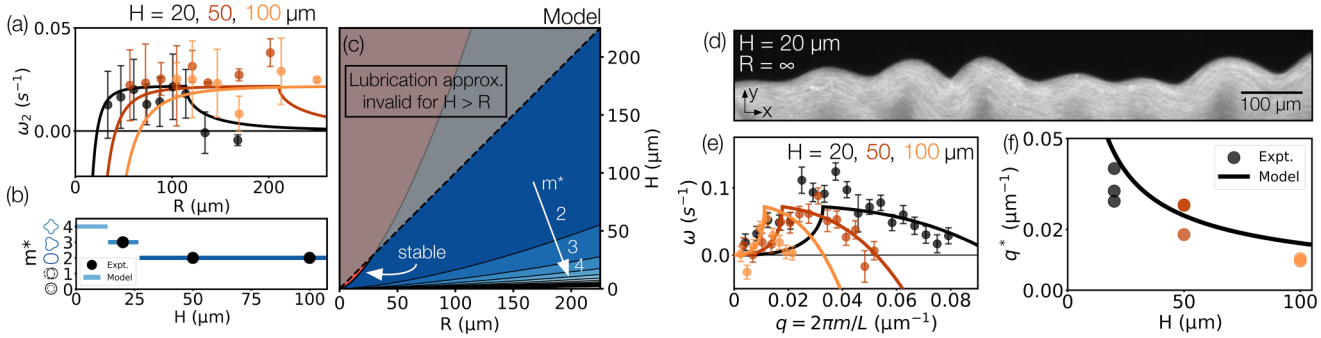


FIG. 3. Fastest-growing mode number m^* and wave number $q^* = 2\pi m^*/L$ decrease with gap height H. (a) Measured growth rates (disks) and model growth rates (lines) for the second radial harmonic at different gap heights. The model parameters are determined by fitting only ω_2 for $H = 20\,\mu$m. (b) Fastest-growing mode number m^* decreases with increasing gap height H for $R = 135\,\mu$m. (c) Phase diagram of the fastest-growing mode number from the model using the parameters in panel (a). (d) Instability at an initially flat active/passive interface. (e) Dispersion relation for a flat interface of length L at different gap heights. The fit parameters are determined by fitting ω only for $H = 50\,\mu$m. (f) Using only the same parameters as in panel (e), we find good agreement between the experiment and model for the fastest-growing wave number q^* as a function of height.

along the plane. Therefore, the resulting equations for the active droplet are (see Appendix A)

$$-\partial_i p + \eta \partial_z^2 u_i - \eta \tau_a^{-1} \partial_z Q_{iz} = 0, \tag{1}$$

$$(\tau_{LC}\partial_t + 1)Q_{iz} - \lambda \tau_{LC} \partial_z u_i = 0, \tag{2}$$

$$\partial_z p = 0, \tag{3}$$

where p is the pressure, u_i is the in-plane velocity ($i = x, y$), Q_{iz} is the iz component of the order parameter tensor, $\lambda \sim 1$ is the flow-tumbling parameter for long slender rods, and η is the shear viscosity of the active and passive fluids (assumed equal for simplicity). We define two timescales for the liquid crystal. First, the active timescale $\tau_a = \eta/a$ decreases when activity a increases and is proportional to velocity autocorrelation time [53]. Second, the liquid crystal timescale τ_{LC} characterizes the relaxation of the order parameter to isotropy. The active/passive interface has the following boundary conditions: the dynamic boundary condition where the jump in normal stress is given by the Laplace pressure, the kinematic boundary condition where the interface moves with the fluid, and the continuity of the normal velocity. We have neglected the Frank elasticity, which is associated with the free energy cost for spatial distortions of Q, and would enter Eq. (2) as a diffusionlike term ($\propto \nabla^2 \mathsf{Q}$). We neglect this term since its contribution does not substantially change our results (Fig. 10). Consequently, Eq. (2) does not require boundary conditions to be imposed for Q. Finally, we assume no-slip boundary conditions on the velocity field at the top and bottom plates.

To study the linear instability of the interface, we assume that the velocity, pressure, and order parameter tensor have time dependence $\exp(\omega t)$. Due to our linearization about the isotropic and quiescent state, and the neglect of Frank elasticity, we can eliminate the order parameter tensor from these equations, which leads to Stokes equations for the velocity with an effective viscosity that depends on the activity (see Appendix A):

$$0 = -\partial_i p + \eta_{\text{eff}} \partial_z^2 u_i, \tag{4}$$

$$\frac{\eta_{\text{eff}}}{\eta} = 1 - \lambda \frac{\tau_a^{-1}}{\omega + \tau_{LC}^{-1}}. \tag{5}$$

Note that for small ω, the effective viscosity decreases with increasing activity, consistent with rheological experiments on microtubule-based active gels [54,55]. When the real part of the effective viscosity is sufficiently negative, there is no resistance to spontaneous shear flow, and active flows drive the deformation of the droplet.

To understand the various timescales at play in the active instability, let us first consider the relaxation of a passive droplet slightly perturbed from its equilibrium shape, with radius $r(\theta, t) = R + h(\theta, t)$, where r and θ are polar coordinates. We use simple scaling arguments to estimate how the relaxation time τ_{HS} of a droplet in a Hele-Shaw (HS) cell depends on the droplet radius R and the gap height H. The balance of the forces arising from the pressure p and the surface tension γ of the interface leads to $p \sim \gamma h/R^2$. The pressure gradient drives a viscous flow, $p/R \sim (\eta/\tau_{HS})(h/H^2)$. Thus, $1/\tau_{HS} \sim \gamma H^2/(\eta R^3)$. Hence, for passive droplets, the relaxation is slower for larger droplets since the driving force—the pressure gradient—is smaller for larger droplets. In contrast, the relaxation is faster for larger gap heights H since the viscous resistance is smaller.

Writing h in a Fourier series $h \propto \cos(m\theta)$, where m is the mode number, reveals how the growth rate of each mode depends on m,

$$\omega_m = -\frac{\eta}{12\tau_{HS}} \frac{m(m^2-1)}{\eta_{\text{eff}} + \eta}, \tag{6}$$

just as in the case of two passive fluids with two viscosities η_{eff} and η [52]. For a passive droplet, all modes decay with $\omega_m < 0$. For an active droplet, η_{eff} is a function of ω [Eq. (5)], which may be complex [56]. Therefore, the real part of the growth rate is positive when the real part $\Re(\eta_{\text{eff}} + \eta) < 0$. As expected, the growth rate vanishes for the dilational mode $m = 0$ due to incompressibility and for the translational mode $m = 1$. For an active droplet, Eq. (6) is an implicit equation for the dispersion relation. Solving for the growth rates, we find

$$\omega_m^{\pm} = \frac{\lambda}{4\tau_a} - \frac{1}{2\tau_{LC}} - \frac{M}{2\tau_{HS}} \pm \sqrt{\left(\frac{\lambda}{4\tau_a} - \frac{1}{2\tau_{LC}} - \frac{M}{2\tau_{HS}}\right)^2 - \frac{M}{\tau_{HS}\tau_{LC}}}, \tag{7}$$

where $M = m(m^2-1)/24$. When the activity vanishes, the two relaxation modes associated with the interface and the liquid crystal are decoupled [Fig. 9(a)]. The liquid crystal relaxes to isotropy without accompanying flows and the motion of the relaxing interface drives a flow. For nonzero activity, these two modes are coupled: flows drive order and order drives flows [Fig. 9(b)]. Above a critical activity, the normal component of the spontaneous flows drives the interfacial instability [Fig. 9(c)]. For a fixed height, there is a critical radius R_c above which the interface is unstable [Fig. 3(c)],

$$R_c = H^{2/3}\left(\frac{\gamma}{\eta}\frac{2M\tau_{LC}\tau_a}{\lambda\tau_{LC} - 2\tau_a}\right)^{1/3}. \tag{8}$$

Similarly, for a fixed radius, there is a critical height below which the interface is unstable [Fig. 3(c)]. In general, the stability of a droplet is determined by two length scales: the geometric gap height and a dynamical scale defined by the capillary velocity together with the active and relaxation timescales.

We find multiple points of agreement between the experiment and model. First, the model quantitatively captures how the mean growth rates of unstable droplets depend on their 3D geometry. When analyzing the effect of droplet radius, we fit the theoretical growth rate of ω_2 [Eq. (7)] to the experimental data [Fig. 2(a)] to determine the parameters τ_a, τ_{LC}, and τ_{HS}. Without modifying these parameters, we find quantitative agreement for the third radial mode [Fig. 2(b)] and the fastest-growing mode [Fig. 2(c)] as a function of droplet radius. For modes greater than three, there are not enough wide droplets to make a statistically significant comparison with our model. Repeating this procedure for varying gap heights, we again find good agreement for the second radial mode [Fig. 3(a)] and the fastest-growing mode [Fig. 3(b)] as a function of droplet radius and gap height. Figure 3(c)

summarizes the opposing contribution of the gap height H and the droplet radius R to the interfacial instability. Second, the model predicts a similar evolution of the shape of individual droplets when starting from the experimental initial conditions for the amplitude and phase of each mode [Figs. 1(d), 1(e), and 7]. The three timescales are $\tau_a \sim 0.5\,\mathrm{s}$, $\tau_{LC} \sim 1\,\mathrm{s}$, and $\tau_{HS} \sim 1$–$1000\,\mathrm{s}$. The relaxation time τ_{HS} varies greatly due to its dependence on droplet radius and gap height. Wide droplets in narrow channels have the longest relaxation time. Our fit value for τ_{HS} yields a capillary speed $\gamma/\eta \sim 10\,\mu\mathrm{m/s}$, which is consistent with previous measurements in similar experimental conditions [28]. Our fit value for τ_a yields an active stress $a \sim 50\,\mathrm{mPa}$, which is consistent with previous measurements of the active stress at a flat quasi-2D active/passive interface [28].

We further demonstrate agreement between our model and experiments by considering the limit of a 2D interface between an active and passive fluid confined between two parallel plates [Fig. 3(d) and Movie S3 in the Supplemental Material [46]]. We observe the growth of an interfacial instability whose fastest-growing wave number q^* is finite [Fig. 3(e)] and decreases with increasing gap height [Fig. 3(f)]. We fit the theoretical growth rates for $H = 50\,\mu\mathrm{m}$ and find good agreement between the model and the experimental dispersion relations at different gap heights [Fig. 3(e)]. Moreover, the model predicts that the fastest-growing wave number of a flat 2D active/passive interface decreases like $q^* \propto H^{-2/3}$ [Eq. (A32)], which is consistent with experimental data [Fig. 3(f)].

III. ACTIVE FLOWS

So far, our investigation has focused solely on interfacial dynamics. Experiments and theory [41] can also probe the nature of active flows driving the interfacial instability. Using particle-image velocimetry, we quantify the active flows inside unstable droplets and find that n-fold symmetric extensional shear flows drive the interfacial instability. Experimental droplets growing modes two and three exhibit predominantly twofold and threefold symmetric shear flows, respectively [Figs. 4(a) and 4(b)]. Since a single extensional shear mode [Figs. 4(c) and 4(d)] does not completely capture the minor asymmetries present in the experimental flows, we consider a superposition of the different extensional shear modes [Figs. 4(e) and 4(f)]. Using the kinematic boundary condition, we establish a linear relationship between the Fourier amplitudes for the flows and the interface [Eqs. (A28) and (A30)]. Using the experimental droplets' interface and the fitted parameters, we reconstruct the instantaneous flows fields for individual droplets with the fastest-growing modes $m^* = 2$ and $m^* = 3$ [Figs. 4(e), 4(f), and 6]. The quantitative agreement between the experiments and our minimal model confirms that the lubrication approximation captures the essential physics underlying the interfacial instability.

IV. DISCUSSION AND CONCLUSION

In summary, we trigger the interfacial instability of confined 3D active droplets using light and as a result are able to study the linear regime, which was previously inaccessible

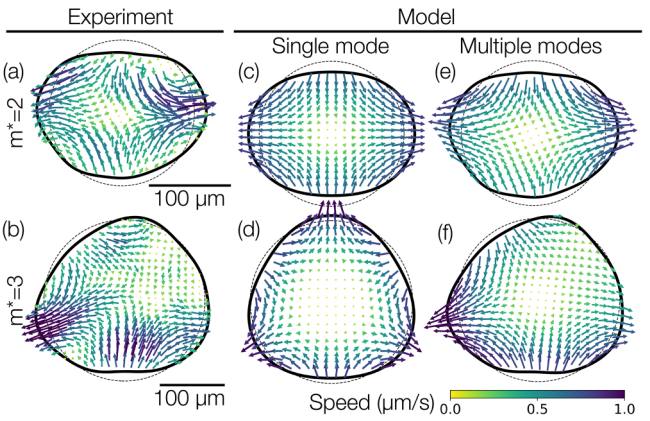


FIG. 4. Extensional shear flow drives interfacial instability ($H = 50\,\mu\mathrm{m}$). In the experiment, interfaces exhibiting mainly the second [panel (a)] and third [panel (b)] radial modes have predominantly dipolar and tripolar extensional shear flow (colored arrows) inside, respectively. (c), (d) The model with a single extensional shear does not fully characterize the irregularities of the experimental active flows. (e), (f) A superposition of the extensional shear modes better capture these features.

for uncontrolled, spontaneous flowing active fluids. Above a critical radius or below a critical thickness, droplets are unstable. The interface grows a superposition of multiple modes, with the dominant one corresponding to the fastest-growing mode and with the same symmetry as the observed active shear flows.

Despite the similarities of the confined geometry and the growth of interfacial radial modes, we find the active instability is fundamentally distinct from the Saffman-Taylor instability, where a less viscous fluid displaces a more viscous fluid. First, in the Saffman-Taylor instability, any external nonzero pressure gradient leads to the fingering instability. Comparatively, the active fluid is driven out of equilibrium internally at the microscopic level. The active interfacial instability occurs only when the activity exceeds a critical (nonzero) value. Second, the active instability occurs regardless of whether we consider an active droplet surrounded by a passive fluid or a passive droplet surrounded by an active fluid (Movie S4 in the Supplemental Material [46]). In contrast, in the Saffman-Taylor instability, the interface is unstable only when the less viscous fluid invades the more viscous fluid. The reverse situation wherein the more viscous fluid invades the less viscous fluid is stable. Finally, the Saffman-Taylor instability is a quasi-2D instability that requires confinement; the deformations vanish for an unconfined 3D droplet or a flat 2D interface. In contrast, 3D active droplets and 2D active/passive interfaces can become unstable even without the Hele-Shaw confining geometry [29,34].

Our model predicts that the onset of the spontaneous flow and the interfacial instabilities occur concurrently at the same critical radius. Still, we find experimentally that the active fluid inside a stable droplet flows spontaneously without deforming the interface. Past experimental work also found that active fluids can spontaneously circulate when confined by solid walls [57] or in droplets with surface tension high enough to prevent deformation [32,58,59]. We only consider

the contribution of the active flows normal to the interface, and therefore our model does not address spontaneous flows that do not deform the interface. Another signature of the coupling of the interfacial and flow instabilities is that the characteristic length scale of the flow depends on surface tension. However, past work on the spontaneous flow instability for an active fluid confined between two parallel plates depends on the channel geometry [43] (but not surface tension because there is no interface present). To better understand the connection between these two instabilities, future work will focus on solving the droplet stability problem in 3D without invoking the lubrication approximation.

ACKNOWLEDGMENTS

We thank Thomas Videbæk and Aparna Baskaran for helpful discussions. We also thank Ray Adkins and Zvonimir Dogic for sharing the experimental protocols. This work was supported in part by the National Science Foundation through Grant No. MRSEC DMR-2011846 (B.C.S., G.D., and T.R.P.), NSF CAREER Awards No. DMR-2047119 (GD) and No. CBET-2227361 (T.R.P. and R.A.P.). This research was also supported in part by NSF through Grant No. PHY-2309135 to the Kavli Institute for Theoretical Physics (KITP) (G.D. and T.R.P.). We also acknowledge the use of the optical, microfluidics, and biomaterial facilities supported by NSF MRSEC Grant No. DMR-2011846. We acknowledge the support of the Natural Sciences Engineering Research Council of Canada (NSERC) [567961-2022] (F.C.). Cette recherche a été financée par le Conseil de recherches en sciences naturelles et en génie du Canada (CRSNG) [567961-2022] (F.C.).

DATA AVAILABILITY

The data that support the findings of this article are not publicly available. The data are available from the authors upon reasonable request.

APPENDIX A: MODEL

In this Appendix, we provide the details of the stability analysis of an initially circular active droplet of radius R with a base state of no flow and no nematic order, surrounded by a passive fluid. We will also consider the limiting case of a very large droplet, which can be approximated by a straight interface between an active fluid and a passive fluid. First, we introduce a minimal hydrodynamic model for the active fluid, along with the boundary conditions at the interface between the active fluid and the passive fluid, as well as at the top and bottom parallel plates. Since we study the growth of small perturbations, we linearize the equations and assume an exponential time dependence. The problem is further simplified by invoking the lubrication approximation for a flow in a thin gap. Finally, we solve for the growth rates of the individual modes corresponding to the Fourier modes of the distortion of the interface and calculate the corresponding flow fields and order parameter fields.

Our minimal hydrodynamical model for the active fluid is [50]

$$-\nabla p + \eta\nabla^2\mathbf{u} - \eta\tau_a^{-1}\nabla\cdot\mathsf{Q} = \mathbf{0}, \tag{A1}$$

$$\tau_{LC}(\partial_t\mathsf{Q} + \mathbf{u}\cdot\nabla\mathsf{Q} + \mathsf{Q}\cdot\Omega - \Omega\cdot\mathsf{Q}) = -\mathsf{Q} + l^2\nabla^2\mathsf{Q} + \lambda\tau_{LC}[2\mathsf{E} + \mathsf{Q}\cdot\mathsf{E} + \mathsf{E}\cdot\mathsf{Q} - 2\mathrm{Tr}(\mathsf{Q}\cdot\mathsf{E})\mathsf{I}], \tag{A2}$$

$$\nabla\cdot\mathbf{u} = 0, \tag{A3}$$

where $\mathbf{u}$ is the velocity field, p is the pressure, $\mathsf{E} = [(\nabla\mathbf{u})^T + \nabla\mathbf{u}]/2$ is the strain rate tensor, $\Omega = [\nabla\mathbf{u} - (\nabla\mathbf{u})^T]/2$ is the vorticity tensor, and Q is the order parameter tensor in three dimensions. Note that our convention is $\mathsf{Q} = S(3\hat{\mathbf{d}}\hat{\mathbf{d}} - \mathsf{I})$, where S is the scalar order parameter, $\hat{\mathbf{d}}$ is the director field, and I is the identity tensor. The parameter η is the shear viscosity, and $\lambda \leqslant 1$ characterizes how the constituent rods align with the principal axes of the strain rate. The correlation length l characterizes how the liquid crystalline order decays in space; the Frank elastic constant is proportional to l^2. The active timescale is $\tau_a = \eta/a$ and is proportional to the velocity autocorrelation time [53]. The timescale τ_{LC} characterizes the relaxation in time of the order parameter to isotropy. We have neglected the Ericksen stress [60] in the modified Stokes equation (A1) for simplicity. We will also neglect the Frank elasticity term for simplicity, which corresponds to taking $l = 0$. Later, we show that including this term does not change the results appreciably. The outer passive fluid is modeled by the Stokes equations,

$$-\nabla p + \eta\nabla^2\mathbf{u} = \mathbf{0}, \tag{A4}$$

$$\nabla\cdot\mathbf{u} = 0. \tag{A5}$$

Since we assume a uniform surface tension γ at the active/passive interface, and disregard any Marangoni stresses that may develop due to impurities at the interface [61], the jump in the stress tensor T is given by

$$\mathbf{n}\cdot(\mathsf{T}^- - \mathsf{T}^+) = \gamma\left(\frac{1}{R_1} + \frac{1}{R_2}\right)\hat{\mathbf{n}}, \tag{A6}$$

where $\mathbf{n}$ is the outward pointing normal at the interface, the superscripts denote the inner $(-)$ and outer $(+)$ fluids, and R_1 and R_2 are the principal radii of curvature of the interface. The stress tensor is given by $\mathsf{T} = -p\mathsf{I} + \eta[\nabla\mathbf{u} + (\nabla\mathbf{u})^T] - a\mathsf{Q}$ (where $a = 0$ for the passive fluid). Since we observe that the interface has very little curvature in the plane perpendicular to the parallel plates [Fig. 1(b)], we take $R_2 = \infty$. The velocity is continuous at the interface, $\mathbf{u}^+ = \mathbf{u}^-$, and is related to the shape of the interface $r = \zeta(\cdot, t)$ via the kinematic condition

$$\partial_t\zeta + \mathbf{u}^+\cdot\nabla\zeta = \mathbf{u}^+\cdot\mathbf{n}. \tag{A7}$$

At the top and bottom plates, we have no-slip boundary conditions on the velocity field. In the following, we do not require boundary conditions for Q because we have neglected the Frank elasticity term.

Linearizing the governing equations for the active fluid about a state of no flow and no order leads to

$$-\nabla p + \eta\nabla^2\mathbf{u} - \eta\tau_a^{-1}\nabla\cdot\mathsf{Q} = \mathbf{0}, \tag{A8}$$

$$(\tau_{LC}\partial_t + 1)\mathsf{Q} - 2\lambda\tau_{LC}\mathsf{E} = 0. \tag{A9}$$

To solve these equations, we assume that p, $\mathbf{u}$, and Q are proportional to $\exp(\omega t)$, where ω is the growth rate of the linear instability to be determined. Note that the growth rate can be real or complex. The imaginary part of the growth rate corresponds to the interface having traveling waves [28,38,62].

In our experiments, the droplets are wide and thin, with thickness equal to the gap height H between the parallel plates, which we assume are located at $z = \pm H/2$. Therefore, we apply a lubrication approximation, which implies that gradients in the velocity across the gap are greater than gradients in the velocity along the plates, $\partial_z \gg \partial_i$, where $i = x$ or y. Then, by the incompressibility condition, $u_i \gg u_z$. Thus, the components $E_{iz} \approx (\partial_z u_i)/2$ are dominant. Using Eq. (A9), we see that $\mathsf{Q} \propto \mathsf{E}$, and hence the Q_{iz} components are also dominant. The governing equations for the active fluid reduce to a quasi-2D flow,

$$-\partial_i p + \eta\partial_z^2 u_i - \eta\tau_a^{-1}\partial_z Q_{iz} = 0, \tag{A10}$$

$$(\omega\tau_{LC} + 1)Q_{iz} - \lambda\tau_{LC}\partial_z u_i = 0, \tag{A11}$$

$$\partial_z p = 0. \tag{A12}$$

A similar result is obtained for the passive fluid,

$$-\partial_i p + \eta\partial_z^2 u_i = 0, \tag{A13}$$

$$\partial_z p = 0. \tag{A14}$$

To solve these equations, assume $u_i(r,\theta,z) = \hat{u}_i(r,\theta)f(z)$ and $Q_{iz}(r,\theta,z) = \hat{Q}_{iz}(r,\theta)g(z)$, and substitute to find

$$\hat{u}_i = \frac{1}{\eta_{\text{eff}} f''}\partial_i p, \tag{A15}$$

$$\hat{Q}_{iz} = \frac{\lambda\tau_{LC}}{\omega\tau_{LC}+1}\frac{1}{\eta_{\text{eff}} g'}\partial_i p, \tag{A16}$$

where

$$\eta_{\text{eff}} = \eta\left(1 - \lambda\frac{\tau_a^{-1}}{\tau_{LC}^{-1}+\omega}\right) \tag{A17}$$

as in Eq. (5). Note that f'' and g' must be constants since $\hat{u}_i$, $\hat{Q}_{iz}$, and p are independent of z. Imposing the no-slip boundary conditions at $z = \pm H/2$ and using Eq. (A11) yields

$$u_i = \left(\frac{z^2}{2} - \frac{H^2}{8}\right)\frac{1}{\eta_{\text{eff}}}\partial_i p, \tag{A18}$$

$$Q_{iz} = \frac{\lambda\tau_{LC}}{\omega\tau_{LC}+1} z\frac{1}{\eta_{\text{eff}}}\partial_i p. \tag{A19}$$

The quasi-2D velocity field u_i is a potential flow [52,63], meaning $\partial_x u_y - \partial_y u_x = 0$. The dominant contribution to the order parameter tensor Q_{iz} is also irrotational in this sense. In this approximation, we do not enforce the tangential part of the dynamical boundary condition [Eq. (A6)] or the tangential part of the continuity of the velocity across the interface. These conditions are fulfilled in a thin boundary layer of thickness $\sim H$ near the interface, which is disregarded in the lubrication analysis [63]. For the passive fluid, $\mathsf{Q} = 0$ and $u_i = (z^2/2 - H^2/8)\partial_i p/\eta$.

We use cylindrical polar coordinates (r,θ,z) for an initially circular droplet. The shape of the perturbed interface is given by $r = \zeta(\theta,t) = R + \sum_m \mathcal{H}_m\cos(m\theta)\exp(\omega_m t)$. Working to first order in the coefficients $\mathcal{H}_m$, the curvature in the xy-plane of the contour of a droplet perturbed by the mth mode is

$$\frac{1}{R_1} = \frac{1}{R} + (m^2-1)\frac{\mathcal{H}_m}{R^2}\cos(m\theta)\exp(\omega_m t). \tag{A20}$$

The pressure field inside and outside of the droplet is harmonic since the flow is incompressible potential flow. Using the normal-normal component of the dynamic boundary condition (A6) to determine the angular dependence of the pressure field, we have

$$p_m = \begin{cases} A_m\left(\dfrac{r}{R}\right)^m\cos(m\theta)\exp(\omega_m t), & \text{for } r < R, \\ B_m\left(\dfrac{r}{R}\right)^{-m}\cos(m\theta)\exp(\omega_m t), & \text{for } r > R. \end{cases} \tag{A21}$$

Continuity of the normal component of the velocity at the interface implies $A_m/\eta_{\text{eff}} = -B_m/\eta$. Working to first order in the small quantities $\mathcal{H}_m$, and dropping terms that are subleading in the lubrication approximation, the normal-normal component of the dynamic boundary condition (A6) becomes

$$p_m^- - p_m^+ = \gamma\frac{m^2-1}{R^2}\mathcal{H}_m\cos(m\theta)\exp(\omega_m t). \tag{A22}$$

To apply the kinematic boundary condition (A7), we linearize and average the velocity over the thin gap,

$$\partial_t\zeta = \frac{H^2}{12\eta_{\text{eff}}}\partial_r p, \tag{A23}$$

which leads to an implicit equation for the growth rate

$$\omega_m = -\frac{\gamma H^2}{12R^3}\frac{m(m^2-1)}{\eta_{\text{eff}}(\omega_m)+\eta} = -\frac{\eta}{12\tau_{HS}}\frac{m(m^2-1)}{\eta_{\text{eff}}+\eta}, \tag{A24}$$

where $\tau_{HS} = \eta R^3/(\gamma H^2)$ is the relaxation time of a droplet in an HS cell. Solving (A24) yields the growth rates

$$\omega_m^{\pm} = \frac{\lambda}{4\tau_a} - \frac{1}{2\tau_{LC}} - \frac{M}{2\tau_{HS}} \pm \sqrt{\left(\frac{\lambda}{4\tau_a} - \frac{1}{2\tau_{LC}} - \frac{M}{2\tau_{HS}}\right)^2 - \frac{M}{\tau_{HS}\tau_{LC}}}, \tag{A25}$$

where $M = m(m^2-1)/24$.

1. Reconstruction of the interface and the flow field

We now describe the method of producing Fig. 1(e) which illustrates the evolution of the interface over time, and Fig. 4 which shows the flow fields inside active droplets. First, we

express Q_{rz} in a Fourier series,

$$Q_{rz}(r,\theta,t) = \sum_m \mathcal{Q}_m m \frac{r^{m-1}}{R^m} \cos(m\theta)\exp(\omega t). \tag{A26}$$

Then, substituting this expression into the governing equation for the Q tensor [Eq. (A11)] along with the corresponding Fourier series for u_r, and using the linearized kinematic boundary condition [Eq. (A7)], we arrive at the following eigenvalue problem:

$$\omega\begin{pmatrix}\mathcal{H}_m\\ \mathcal{Q}_m\end{pmatrix} = \begin{pmatrix} -\frac{m}{2\eta}\frac{\gamma(m^2-1)}{R^3}\frac{H^2}{12} & -\frac{m}{2\tau_a}\frac{H^2}{12R} \\ \frac{\lambda}{2\eta}\left(\frac{\gamma(m^2-1)}{R^2}\right) & -\frac{1}{\tau_{LC}}+\frac{\lambda}{2\tau_a}\end{pmatrix}\begin{pmatrix}\mathcal{H}_m\\ \mathcal{Q}_m\end{pmatrix}, \tag{A27}$$

whose eigenvalues are the growth rates [Eq. (A25)]. We normalize the associated eigenvectors of the eigenvalues $\omega_m^{\pm}$ to be of unit length, and denote them by $(\mathcal{H}_m^{\pm}, \mathcal{Q}_m^{\pm})^T$. In general, the interfacial radial perturbation h, the rz component of the order parameter tensor Q_{rz}, and the radial flow velocity u_r inside the droplet are given by a linear combination of the solutions corresponding to the two growth rates $\omega_m^{\pm}$ for each mode,

$$h = \sum_{m=2}^{\infty}[c_m^+\mathcal{H}_m^+\exp(\omega_m^+ t) + c_m^-\mathcal{H}_m^-\exp(\omega_m^- t)] \times \cos(m\theta+\phi_m), \tag{A28}$$

$$Q_{rz} = \sum_{m=2}^{\infty}[c_m^+\mathcal{Q}_m^+\exp(\omega_m^+ t) + c_m^-\mathcal{Q}_m^-\exp(\omega_m^- t)] \times m\frac{r^{m-1}}{R^m}\cos(m\theta+\phi_m), \tag{A29}$$

$$u_r = \sum_{m=2}^{\infty}[c_m^+\mathcal{H}_m^+\omega_m^+\exp(\omega_m^+ t) + c_m^-\mathcal{H}_m^-\omega_m^-\exp(\omega_m^- t)] \times \frac{r^{m-1}}{R^{m-1}}\cos(m\theta+\phi_m), \tag{A30}$$

where $c_m^{\pm}$ are unknown constants that are determined from the initial conditions and ϕ_m are the phases of each mode m. In our experiments, we measure the interfacial deformation and the flow field inside the droplet at some time t. We do not measure the order parameter tensor Q. Fourier decomposition of these measurements yields, for each mode m, the data for the interfacial deformation amplitude h_m, the phase ϕ_m, and the radial velocity component $u_{r,m}$ evaluated at selected grid points (r,θ) within the droplet interior. In an ideal, noise-free setting, solving the linear system constructed from h_m and $u_{r,m}$ at any single grid point suffices to uniquely determine values for the coefficients $c_m^{\pm}$ for each m. These coefficients would then automatically satisfy Eqs. (A28) and (A30) at all other points. In practice, however, noise, measurement inaccuracies, and other sources of experimental error in both the interface and flow field data prevent us from finding values of $c_m^{\pm}$ that satisfy Eqs. (A28) and (A30) at every point (r,θ) simultaneously. Instead, we find $c_m^{\pm}$ approximately using least squares to solve an overdetermined system formed by Eqs. (A28) and (A30) evaluated at all grid points inside a disk of radius $\mathcal{R} < R$. We restrict our analysis to this smaller disk because the flow field measurements near the interface are significantly less reliable than those taken in the bulk. Note, in the event of degenerate eigenvalues, the problem reduces to finding the combined sum $c_m^+ + c_m^-$; that is, only a single effective coefficient needs to be determined. For simplicity, we choose $c_m^+ = 0$ when the eigenvalues are degenerate.

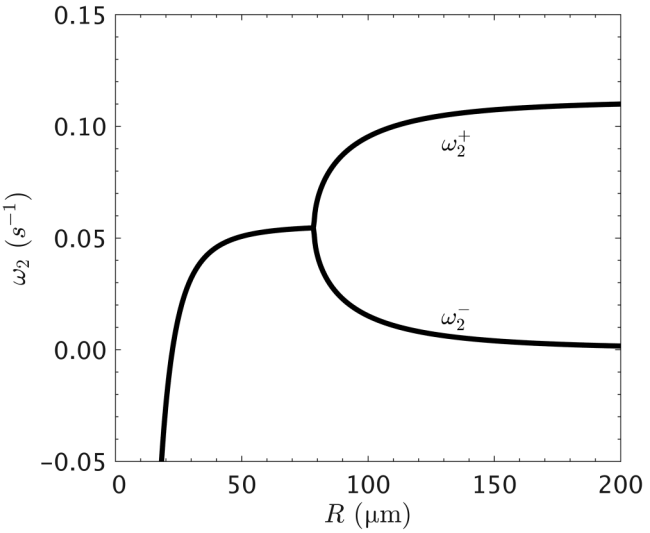


FIG. 5. Real part of the growth rate ω_2 showing both branches ω_2^+ and ω_2^- as a function of the droplet radius R. For $R \sim 80\,\mu$m, the real parts of the two growth rates change from being equal to distinct. The parameters used to produce this figure are the active time $\tau_a = 0.39$ s, the liquid crystal time $\tau_{LC} = 0.86$ s, and the capillary velocity $\gamma/\eta = 12.4\,\mu$m/s. Details on how these parameters are determined are provided in the section on parameter estimation.

Our theory predicts that there are two growth rates $\omega_m^{\pm}$ which couple the instability of the interface with the instability of the liquid crystal. For a given mode m, $\omega_m^{\pm}$ can be real or complex, depending on the sign of the discriminant. When the discriminant is negative, the growth rates $\omega_m^{\pm}$ occur in complex conjugate pairs, where the imaginary part implies that there are traveling waves on the interface. While the study of such waves is beyond the scope of this paper, other authors have observed the possibility of traveling waves occurring on the surface of active liquid crystals [28,38,62]. Since the imaginary part of the growth rates is not measured, we ignore it in the model analysis for simplicity. When the discriminant is positive, the growth rates are real and distinct. In Fig. 5, we plot the real part of the growth rates of the second mode number. The real parts of the growth rates are equal until $R \sim 80\,\mu$m, after which they split into two distinct branches. We denote the top branch as plus and the bottom branch as minus.

Due to limited experimental resolution, we cannot conclusively determine whether the dynamics of the interface are best described by a single or double exponential. However, the vast majority of the experimental data lie in the region where the growth rates have equal real part; i.e., there is only one growth rate. For $m = 2$, this occurs for $R \lesssim 80\,\mu$m

[Fig. 2(a)]. There are significantly fewer experimental data points in the region where the model predicts the growth rates have distinct real parts. Therefore, the issue of the coupling between the two growth rates is not a major factor in our fitting and analysis. Moreover, when the growth rates are distinct, the behavior of the minus branch of the growth rates matches qualitatively with the experimentally observed growth rates. This match is seen in Fig. 2(a), where the binned growth rates increase with radius up to $R \sim 80\,\mu$m, after which the growth rates decrease and is *qualitatively* identical to the behavior of ω_m^-, not ω_m^+ (see Fig. 5 for the comparison of ω_m^+ versus ω_m^-). Thus, we estimate the unknown parameters—the active time (τ_a), the liquid crystal relaxation time (τ_{LC}), and the capillary velocity (γ/η)—by fitting the experimental growth rate data with the ω_m^- branch of the model.

2. Straight interface limit

The flows in our lubrication theory are potential flows. Therefore, when the fastest-growing mode m^* is small, the characteristic length scale of the flow in a finite droplet is the radius R of the droplet. When the droplet becomes so large that $m^* \gg 1$, the flow velocity decays exponentially and radially inward with a length scale comparable to the wavelength of the distortion of the slightly curved interface. In this very large limit, where $m^* \gg 1$, the interface can be approximated by a straight interface between the active and passive fluid. The wave number is defined in terms of the droplet radius and mode number, $q = m/R$. Then, defining a dimensionless wave number $k = qH$, the growth rates for the straight interface are determined by taking the limit $R \to \infty$,

$$\omega^{\pm} = \frac{\lambda}{4\tau_a} - \frac{1}{2\tau_{LC}} - \frac{1}{2}\beta k^3 \pm \sqrt{\left(\frac{\lambda}{4\tau_a} - \frac{1}{2\tau_{LC}} - \frac{1}{2}\beta k^3\right)^2 - \frac{\beta k^3}{\tau_{LC}}}, \tag{A31}$$

where $\beta = \frac{1}{24}\frac{\gamma}{\eta}\frac{1}{H}$.

The fastest-growing wave number q^* is determined when the discriminant of the growth rate equation is zero,

$$q^* = H^{-2/3}\left[\frac{24}{\gamma/\eta}\left(\frac{\lambda}{2\tau_a} + \frac{1}{\tau_{LC}} + \sqrt{\frac{2\lambda}{\tau_a\tau_{LC}}}\right)\right]^{1/3}. \tag{A32}$$

We use this equation to produce the model prediction of the fastest-growing wavelength in Fig. 3(f). See the parameter estimation section for the details of how the parameters were determined.

3. Parameter estimation

We find three sets of optimal parameter values for the active timescale τ_a, the liquid crystal relaxation time τ_{LC}, and the capillary velocity γ/η. We determine the parameter values by minimizing the weighted sum of squares of the difference of the growth rates between the model and experiment. The minimization algorithm we use is fmincon combined with multistart (to avoid local minima) in MATLAB. The weights are given by the inverse of the variances. For robustness, we also sweep over the parameters τ_a, τ_{LC}, γ/η to find the optimal values and compare with the results produced by fmincon.

In Fig. 2(a), the average growth rates are computed by binning the growth rates by their radius and averaging over each bin. For all of these droplets, the gap height is $H = 20\,\mu$m. The optimal parameter values are found by minimizing the difference of the bin-averaged growth rates of the second mode number with the model-predicted growth rates of the second mode number [Eq. (A25)] across a range of bin radii. The optimal parameters are determined to be $\tau_a = 0.39$ s, $\tau_{LC} = 0.86$ s, and $\gamma/\eta = 12.4\,\mu$m/s. We use these parameters to plot the growth rates shown in Fig. 5, the growth rates of the third mode number and the fastest-growing mode [Figs. 2(b) and 2(c), respectively], and the evolution of the interfacial deformation [Fig. 1(e)]. To generate Fig. 1(e), we measure the deformation of the interface and the flow field at $t = 35$ s taken from the beginning of the linear instability for five cases: a droplet that is predominantly stable, and droplets that have the fastest-growing mode number $m^* = 2, 3, 4$, and 5 in a gap height of $20\,\mu$m. In each case, Fourier decomposition yields the data h_m, $u_{r,m}$, and ϕ_m. Revisiting Eqs. (A28) and (A30), we determine the coefficients $c_m^{\pm}$ by using least squares to solve the overdetermined system as previously described in the section on reconstruction of the interface and the flow field. Finally, measuring the initial amplitudes of the interfacial deformation, we use Eq. (A28) and march forward in time to produce Fig. 1(e).

We also reconstruct the model-predicted flow fields to compare with experimentally measured flows. Using Eq. (A30), Fig. 6 presents a comparison between the experimental and model-predicted flow fields at $t = 35$ s, based on the evolved interfacial deformation for droplets exhibiting the fastest-growing mode number $m^* = 2, 3, 4, 5$ in a $20\,\mu$m gap.

We observe in Fig. 6 that the measured interfacial deformation at $t = 35$ s aligns remarkably well with the model prediction obtained by evolving the initial state. This agreement is further quantified by directly comparing the measured and predicted amplitudes at $t = 35$ s (Fig. 7).

In Fig. 3(a), the experimental configurations are different than in Fig. 2(a): The concentration of ATP, and consequently the activity, in Fig. 3(a) is lower. Hence, we cannot reuse the parameters that were determined for Fig. 2(a). Instead, we refit the parameters [following the same minimization principle as in Fig. 2(a)] for a different set of growth rate data for droplets in a $H = 20\,\mu$m gap height. The optimal parameters are determined to be $\tau_a = 0.37$ s, $\tau_{LC} = 0.73$ s, $\gamma/\eta = 5.10\,\mu$m/s. These parameters are then used to generate the model growth rate curves ω_2^- for the $50\,\mu$m and $100\,\mu$m gap heights in Fig. 3(a), the fastest-growing mode number m^* in Fig. 3(b), and the comparisons of the reconstructed interface and flow field with that of the experiment in Figs. 4(e) and 4(f). To generate Figs. 4(e) and 4(f), we measure the deformation of the interface and the flow field at $t = 50$ s after the onset of the linear instability for two cases: a droplet that is predominantly mode 2 [Fig. 4(a)] and a droplet that is predominantly mode 3 [Fig. 4(b)]. The gap height is $50\,\mu$m. In each case, Fourier decomposition yields the data h_m, $u_{r,m}$, and ϕ_m. Following the same procedure outlined previously in the reconstruction of the interface and the flow field section, we determine the

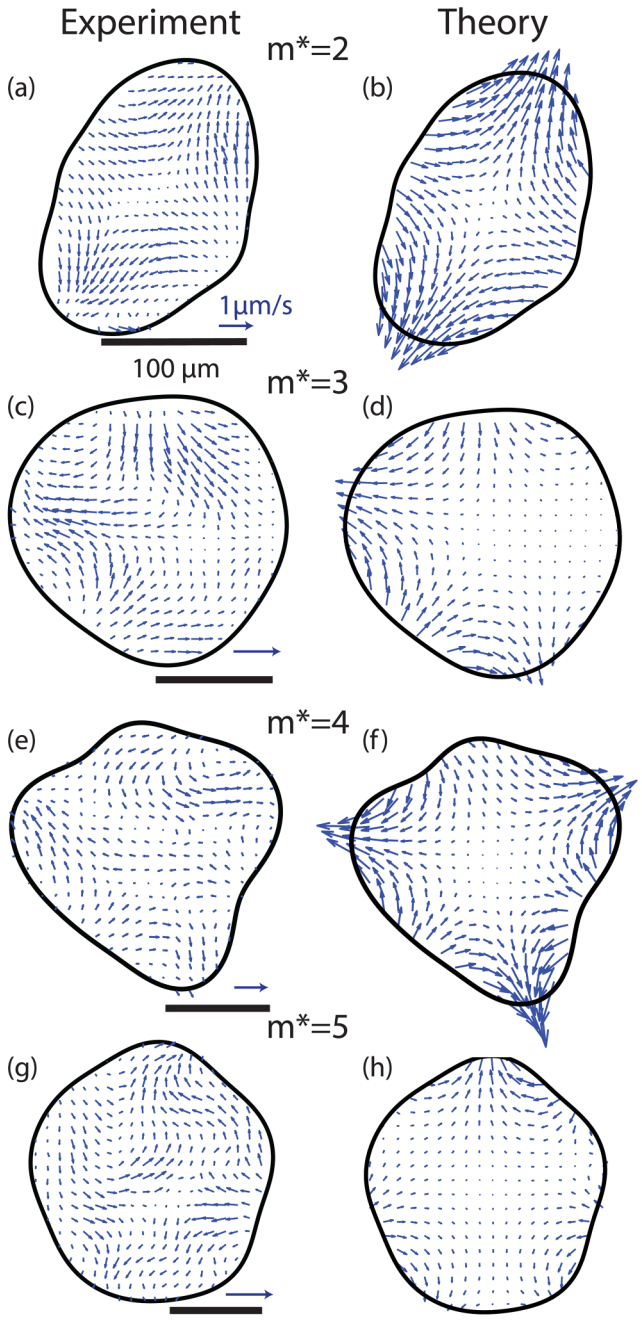


FIG. 6. Reconstruction of the interfacial deformation and flow fields at $t = 35$ s from the onset of instability for droplets of fastest-growing mode $m^* = 2, 3, 4, 5$, from top to bottom. Panels (a), (c), (e), and (g) show the measured flow fields from experiment, while panels (b), (d), (f), and (h) show the model-predicted flow fields.

coefficients $c_m^{\pm}$ by using least squares to solve the overdetermined system. Hence, using Eqs. (A28) and (A30), we reconstruct the flow fields and interfacial deformation at $t = 50$ s [Figs. 4(e) and 4(f)]. Figures 4(e) and 4(f) show good qualitative agreement between the experimental and model-reconstructed flow fields, and this is further reflected when comparing the distribution of their flow speeds (Fig. 8).

For the straight interface in Fig. 3(e), we minimize the weighted sum of squares of the difference of the model growth rates of the minus branch ω^- with the growth rates of the straight interface for *only* the 50 μm gap height. The optimal parameters are $\tau_a = 0.49$ s, $\tau_{LC} = 1.14$ s, and $\gamma/\eta = 9.9$ μm/s. We use these parameters to generate the model growth rate curves for the $H = 20$ and 100 μm gap heights in Fig. 3(e) and the fastest-growing wave number in Fig. 3(f).

4. Activity couples the growth rates

We show the effect of activity on the coupling of the growth rates in the straight interface case. The critical activity for the instability is determined by considering when the real part of the growth rate changes sign, $\Re(\omega_m^{\pm}) = 0$. We define a dimensionless activity α in terms of the active timescale τ_a and liquid crystal timescale τ_{LC}, $\alpha = \lambda\tau_{LC}/\tau_a = \tau_{LC}/\tau_a$, since in our system $\lambda = 1$. Therefore, the critical dimensionless activity is

$$\alpha_c = \frac{\tau_{LC}}{\tau_a} = 2 + 2k^3\tau_{LC}\beta. \tag{A33}$$

A comparison of the growth rates of the straight interface versus the wave number q for zero activity, positive activity but below the critical activity, and above the critical activity is shown in Fig. 9. In the case of zero activity, the relaxation rate of the interface and the liquid crystalline order are decoupled. By mass conservation, because the interface cannot have dilation at zero wave number, we know that the black curve passing through $\omega = 0$ must represent the relaxation of the interface. Once the activity is turned on, both growth rate branches contribute to the instability of the interface and liquid crystal; this is described by Eqs. (A28) and (A29).

5. Neglecting the Frank elasticity

The nematic correlation length l is proportional to the square root of the Frank elastic constant. In our model, we neglect the Frank elastic constant by taking $l = 0$. We justify this approximation because (1) the dispersion relation with the Frank elasticity included is complicated and does not yield a closed form expression for the growth rates and (2) neglecting the Frank elasticity does not substantially change the results; it only requires a higher value of activity in order to achieve a qualitatively similar growth rate curve. Unlike the case of $l = 0$, where no boundary conditions on Q are needed, we now impose torque-free boundary conditions for Q at the top/bottom plates. The dispersion relation can be determined by following similar steps as in the $l = 0$ case. Comparing the growth rates of the straight interface for a range of correlation lengths, we find that for nonzero l, the activity must be increased in order to achieve the same qualitative behavior, but with the merge point of the real part of the growth rates shifting to a smaller wave number q, as shown in Fig. 10. We reuse the parameters $\tau_{LC} = 1.14$ s and $\gamma/\eta = 9.9$ μm/s as determined from Fig. 3(e). For $l = 0$, the critical dimensionless activity is $\alpha_c = 2.34$, while for $l = 25$ and 50 μm, $\alpha_c = 7.16$ and 21.7, respectively.

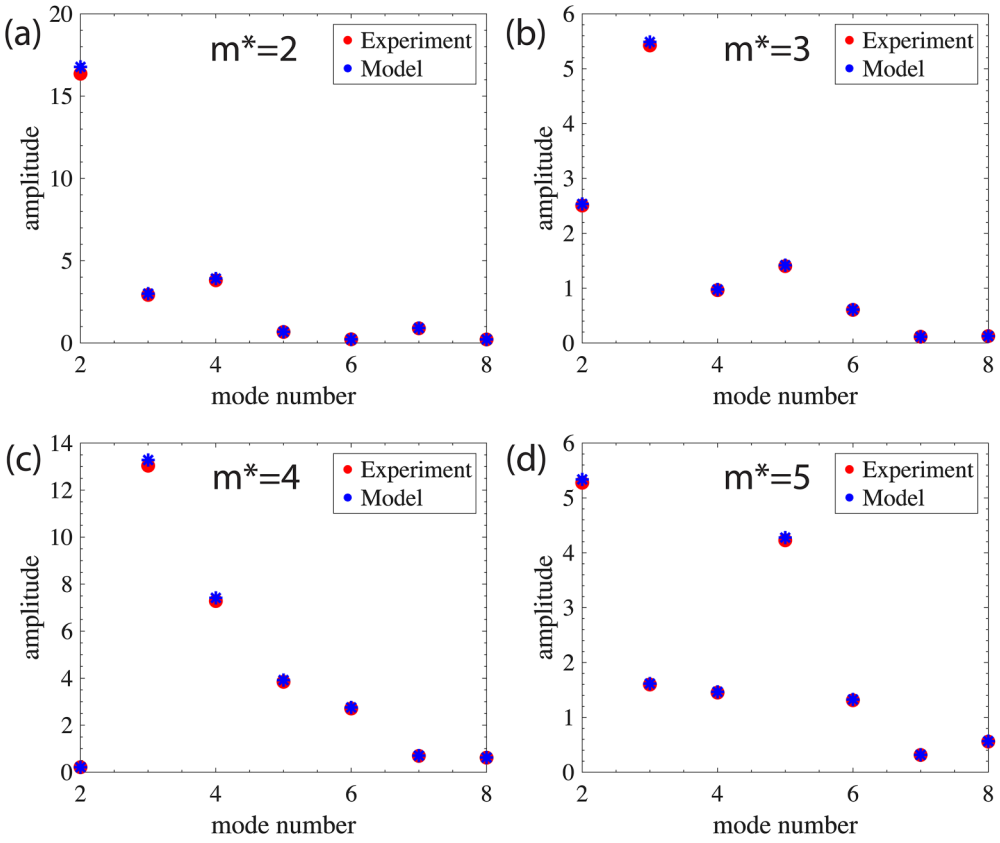


FIG. 7. Comparison of the measured interfacial deformation amplitudes (red circles) at $t = 35$ s with model-predicted amplitudes evolved from the initial state (blue stars), shown as a function of mode number m for droplets of fastest-growing mode (a) $m^* = 2$, (b) $m^* = 3$, (c) $m^* = 4$, and (d) $m^* = 5$.

APPENDIX B: EXPERIMENTAL MATERIALS AND METHODS

1. Microtubules and Kinesin Motor Clusters

Microtubules and kinesin motor clusters were purified and assembled as was done in Chandrakar *et al.* [43]. In summary, microtubules are assembled from tubulin dimers that are purified from bovine brains. Microtubules are polymerized with 3% Alexa647 labeled tubulin, and GMPCPP (a nonhydrolyzable GTP analog) to stabilize microtubules against depolymerization. Kinesin motor clusters are assembled from the processive, biotinylated motors K401-BIO-6xHIS and streptavidin.

2. Active and passive fluids

The PEG-rich and Dextran-rich fluids are assembled as was done in Adkins *et al.* [28]. To begin, 50 ml solutions of 18.81% Dextran (Sigma-Aldrich Dextran from Leuconostoc mesenteroides 1.5–2.8 mDa) in water and 12% PEG

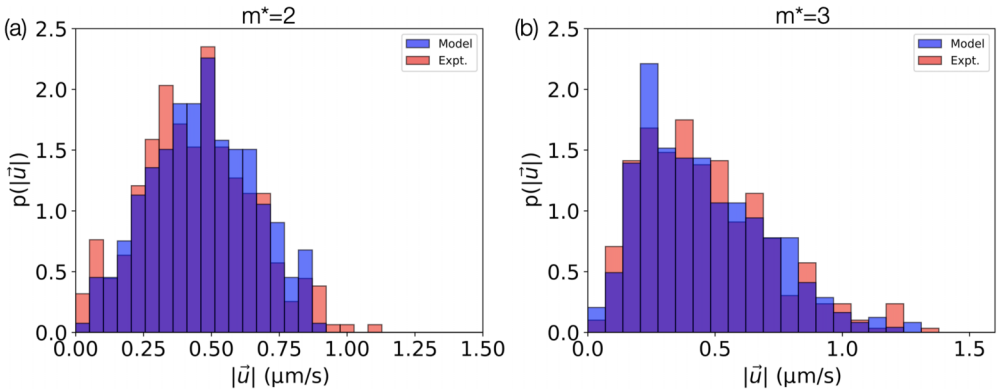


FIG. 8. Flow speed distributions. Using the parameters determined in Fig. 3(a), we construct the flow fields inside individual droplets that grow (a) $m^* = 2$ and (b) $m^* = 3$, respectively, and measure the distribution of flow speeds within the individual droplets. In both cases, we find good agreement in the distribution of flow speeds between experiment and theory.

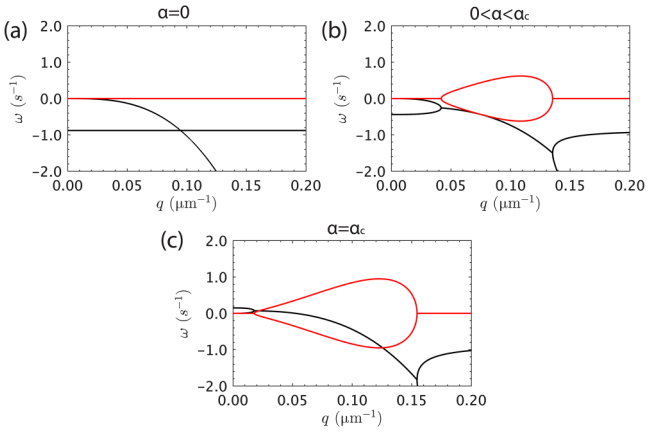


FIG. 9. Growth rates ω vs the wave number q for an initially straight interface for various activity values: (a) zero activity, (b) positive but subcritical activity, and (c) critical activity. The black curves denote the real part of the growth rate $\Re(\omega)$ and red curves denote the imaginary part $\Im(\omega)$. In all of these plots, we use the parameters $\tau_{\rm LC} = 1.14\,$s, $\gamma/\eta = 9.9\,\mu$m/s originally determined by fitting the growth rates from the straight interface for the 50 μm gap height [Fig. 3(e)]. Zero activity [panel (a)] results in a decoupled relaxation of the fluid-fluid interface and the q-independent relaxation of the order of an isotropic liquid crystal with no Frank elasticity.

(Sigma-Aldrich 35 kDa) in M2B are prepared. M2B is a high-molarity PIPES (1,4-piperazinediethanesulfonic) buffer. Then, a "premix" solution of the reagents enumerated below is prepared (Table I). Given that the phase separation is sensitive to the concentrations of the reagents, using a balance is more accurate than using a pipette to control the composition of the premix. Once the premix is prepared, it is aliquoted in to 45 μl samples and flash frozen for later usage. On the day an experiment is performed, the active sample is prepared by adding microtubules, motor clusters, caged ATP, and bovine serum albumin (BSA) to the premix (Table I).

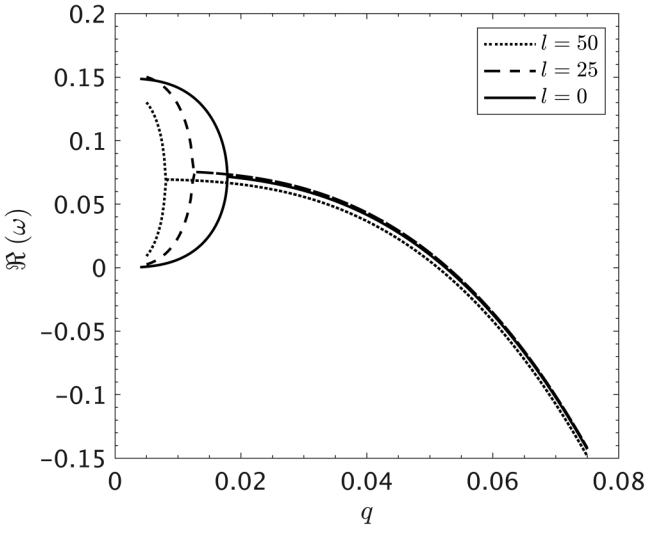


FIG. 10. Growth rates of the straight interface as a function of wave number q for nematic correlation lengths $l = 0, 25, 50\,\mu$m. The correlation length is proportional to the square root of the Frank elasticity. For $l = 0$, we use the same parameters as determined for Fig. 3(e). In order to achieve a similar qualitative behavior for nonzero Frank elasticity, the critical dimensionless activity α_c needs to be increased. For $l = 25, 50\,\mu$m, α_c needs to be increased by a factor of ∼3, 9, respectively. Including the Frank elasticity shifts the merge point of the two branches to a smaller value of q, but otherwise does not substantially change the qualitative behavior of the growth rates.

TABLE I. Reagent mixtures used in premix, active mix, and kinesin-streptavidin assembly (KSA).

Premix	
Reagent	Mass (mg)
M2B	497.59
PEG 10% in M2B (35 kDa)	996.72
Dextran 18.81% in H_2O (1.5–2.2 MDa)	557.78
10× M2B	55.78
AO1 (300 mg/ml glucose + 0.5 M DTT)	116.28
AO2 (20 mg/ml glucose oxidase + 3.5 mg/ml catalase)	116.28
PEP (200 mM)	699.45
Trolox (20 mM)	524.59
PK/LDH	148.63
Mix (933 μl M2B + 67 μl $MgCl_2$ 1 M)	253.55
Active mix	
Reagent	Mass (mg)
Premix	36.6
Microtubules (8 mg/ml)	4.0
KSA (0.7 mg/ml)	2.5
NPE-caged ATP (40 mM)	3.7
BSA (90 mM)	3.7
Kinesin-streptavidin assembly	
Reagent	Volume (μl)
Kinesin (1.2 mg/ml)	5.0
Streptavidin	5.7
DTT (10 mM)	0.5

3. Surface treatment

The surface treatment is *extremely* important to observing the interfacial instability. The top and bottom glass substrates are PEGylated to prevent the Dextran-rich droplets from pinning to the surface from pinning to the surface, as shown in Fig. 11. Without the surface treatment, the Dextran-rich droplets are pinned to the surface and while active flows are observed inside the droplet, there are no interfacial fluctuations. When the surface is properly treated, Dextran-rich active droplets slide along the PEGylated surface. A good indicator that the surface treatment succeeded is that two coalescing active droplets relax to a circular droplet.



FIG. 11. Schematic of the PEGylated surface treatment which prevents Dextran-rich droplets from pinning to the glass substrate.

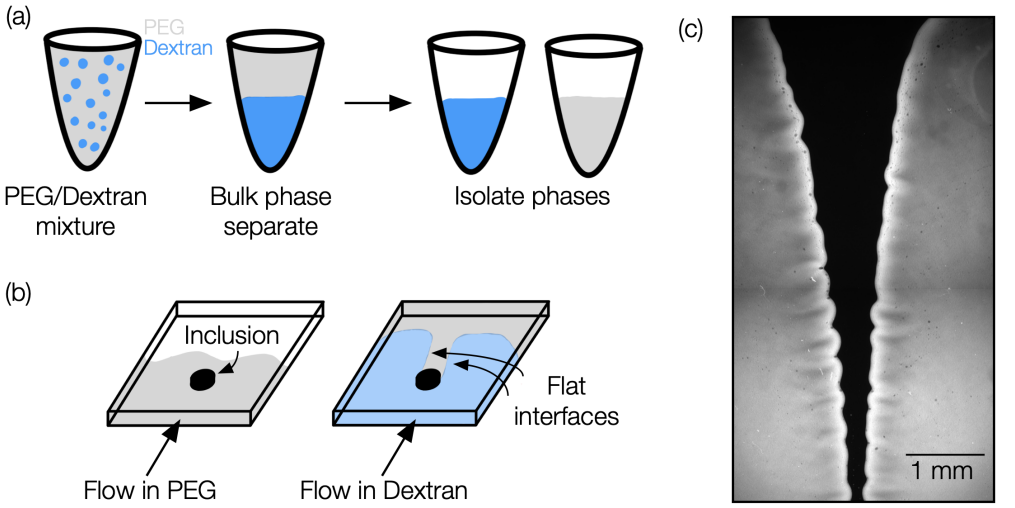


FIG. 12. Construction of an initially flat active-passive interface. (a) PEG-rich and Dextran-rich liquids are bulk phase separated with centrifugation and isolated into different tubes. (b) A Hele-Shaw cell with a small inclusion. First, the PEG-rich fluid is flowed in, followed by the Dextran-rich fluid (which contains the microtubules and molecular motors). (c) Two experimental snapshots stitched together to show the active/passive interface during the interfacial instability.

The surface treatment process has two steps: (1) creating the PEGylated surface and (2) sonicating off excess PEG. The standard acrylamide surface treatment is prepared as done in Lau *et al.* [64] by cleaning the glass substrate, silanizing the surface, and soaking the silanized glass in a solution of monomeric acrylamide which polymerizes off the surface. To create the PEGylated surface, we make the following modification: the 2% acrylamide solution (Sigma-Aldrich) the glass slides incubate within is replaced with 1.5% acrylamide and 0.5% PEG acrylate (Sigma-Aldrich Poly(ethylene glycol) methyl ether acrylate 480 Da). Let the glass slides incubate in solution for 24 h. After 24 h, the solution will be very viscous from the long chains of polymerized PEG. Dispose of the viscous PEG solution and pour water into the glass slide containers. Then, sonicate the glass slides for 8–24 h to fully remove all the excess PEG and leave behind only the PEG acrylate which is attached to the acrylamide substrate. Care must be taken that the water in the sonicator does not get too hot as this can damage the surface treatment. Replace the water in the glass container roughly every hour. The glass slides are fully clean when (1) no residual PEG gel is stuck to the surface and (2) a water droplet uniformly wets the surface. Once clean, store the glass slides in water; they are good for up to one month. Although tedious, cleaning the PEGylated surface is the most important step in obtaining active droplets.

4. Construction of confined active droplets and the initially flat interface

The Hele-Shaw cell is constructed using the PEGylated glass slides and cover slips as well as double-sided tape (3M) of different widths to set the gap height. Two-part epoxy (Devcon) is used to seal the channel; UV-curable glue cannot be used in conjunction with UV-activable ATP.

Active droplets are readily made by flowing the mixture of PEG/Dextran and the active ingredients into a Hele-Shaw cell. Constructing an initially flat active/passive interface is more challenging. First, PEG and Dextran are bulk phase separated with centrifugation and isolated into different tubes. Then, during the assembly of the Hele-Shaw cell we add a small inclusion. This could be a piece of parafilm or double sided tape. In our case, we used a fine-tipped Sharpie to create a dot on the glass slide which still acts like a solid barrier to the PEG-rich and Dextran-rich fluids. The PEG-rich fluid is flowed into the Hele-Shaw cell, followed by the Dextran-rich fluid (which contains the microtubules and molecular motors), as shown in Fig. 12. The resulting active/passive interfacial is initially flat and microtubules are aligned along the interface due to the shear flow they experience when being flowed in.

5. UV illumination

The instability is triggered by exposing the sample to ultraviolet light which uncages ATP. Ultraviolet illumination is produced using a commercial lamp (MelodySusie) with wavelength $\lambda = 365$ nm and intensity 35 W. We illuminate the sample for 35 s. The uncaging of ATP is not an all-at-once process but rather a photochemical process. We find 30+ s of UV illumination at 35 W is sufficient for most of the ATP to be released. Reilluminating the sample with ultraviolet light after the initial illumination does not cause noticeable changes in the fluid's activity, suggesting that the majority of usable ATP has been released.

The system is saturated in caged ATP, so small variations in the concentration of caged ATP used does not affect the available fuel for the molecular motors. However, we do observe that the fluid's activity is sensitive to the concentration of caged ATP, likely because caged ATP is provided as a disodium salt, and salt is known to affect the activity of the microtubule-based active fluid. By weighing out the mass of

TABLE II. Droplet counts in each bin for Fig. 2.

Radius	21	29	37	45	54	62	70	79	87	95	103	112	120	135
Count	278	103	83	66	46	30	25	10	6	9	4	2	2	1

TABLE III. Droplet counts in each bin for Fig. 3.

$H = 20\,\mu$m		$H = 50\,\mu$m		$H = 100\,\mu$m	
Radius	Count	Radius	Count	Radius	Count
34	102	56	89	105	15
47	108	73	27	121	11
60	59	89	14	147	2
74	31	105	12	169	6
87	13	121	2	213	3
101	10	137	2	250	2
114	4	153	1		
134	6	169	6		
168	3	202	2		
		250	1		
		298	1		

caged ATP used each time, we are accurate in the concentration of caged ATP used. Beyond ATP and salt concentration, the strength of the active flows is largely determined by the concentration of molecular motors as they are the force generators in the active liquid crystal.

6. Droplet Size Distribution

The droplet size distribution accessible in experiments limits our observation of unstable droplets whose fastest wave number is $m^* = 4$ or greater [Fig. 2(c)]. The droplet size distribution is set primarily by the volume fractions of PEG and Dextran and secondarily the gap height (Fig. 13). Larger gap heights tend to have larger droplets (Figs. 13 and 14). The sparsity of droplets that have radii much bigger than their gap heights motivated us to investigate the instability of an initially flat interface in different gap heights because it is not affected by the limitations of the droplet size distribution.

We cannot simply increase the volume fraction of Dextran to observe larger droplets during the instability. Recall that before the caged ATP is released, the microtubule network is a rigidly cross-linked gel, which sometimes leads to droplets that are not initially circular (Movie S1 in the Supplemental Material [46]). Larger droplets are more prone to such imperfections. The volume fractions of PEG and Dextran were chosen to bolster the number of droplets that begin initially circular while trying to get the biggest droplets possible.

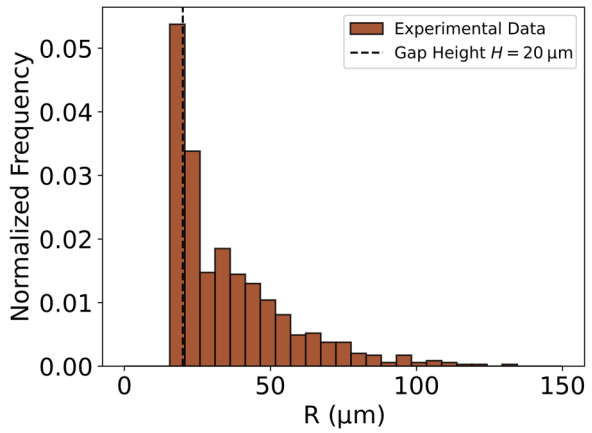


FIG. 13. Droplet size distribution for the experiments present in Fig. 2.

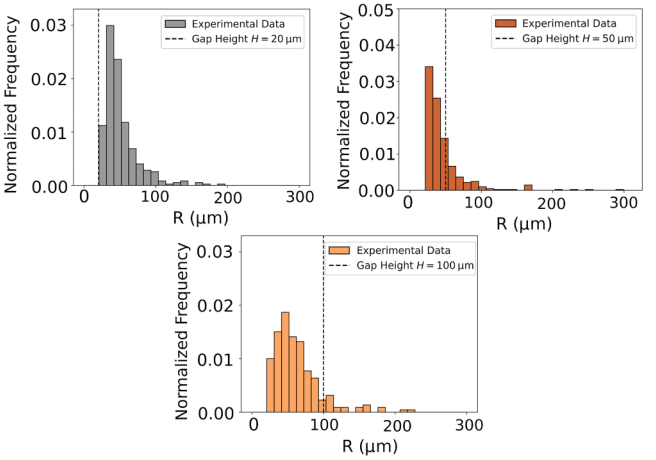


FIG. 14. Droplet size distributions in gap widths of varying height for the experiments presented in Fig. 3.

In Fig. 2, the number of droplets in each bin is presented in Table II. Bins with only one droplet are not plotted as an error bar in Fig. 2. The size distribution is shown in Fig. 13.

In Fig. 3, the number of droplets in each bin is shown in Table III. Again, bins with only one droplet are not plotted as an errorbar in Fig. 3. The size distribution is shown in Fig. 14.

As a consequence of the limited number of wide droplets, our measurement of the fastest-growing mode versus gap height is limited. Comparing the fastest-growing mode m^* at fixed radius versus gap height requires the droplet radius be larger than the largest gap height (to satisfy the lubrication approximation), but the number of such droplets is limited. If we consider $R \approx 135\,\mu$m and $H = 20, 50, 100\,\mu$m, we have better statistics on the number of droplets at each gap height [Fig. 15(a)] than if we consider $R \approx 200\,\mu$m and $H = 20, 50, 100, 200\,\mu$m [Fig. 15(b)]. The small sample size may be skewing the data at $H = 200\,\mu$m.

7. Measurement of negative growth rates in experiment

Accurate measurement of a negative growth rate requires resolving the incipient perturbation to the fluid interface and

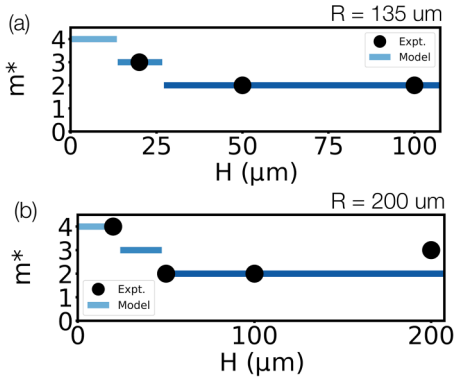


FIG. 15. Fastest-growing mode number m^* vs gap height H for (a) $R = 135\,\mu$m and (b) $R = 200\,\mu$m. There are fewer droplets of larger sizes, which may skew the $H = 200\,\mu$m results.

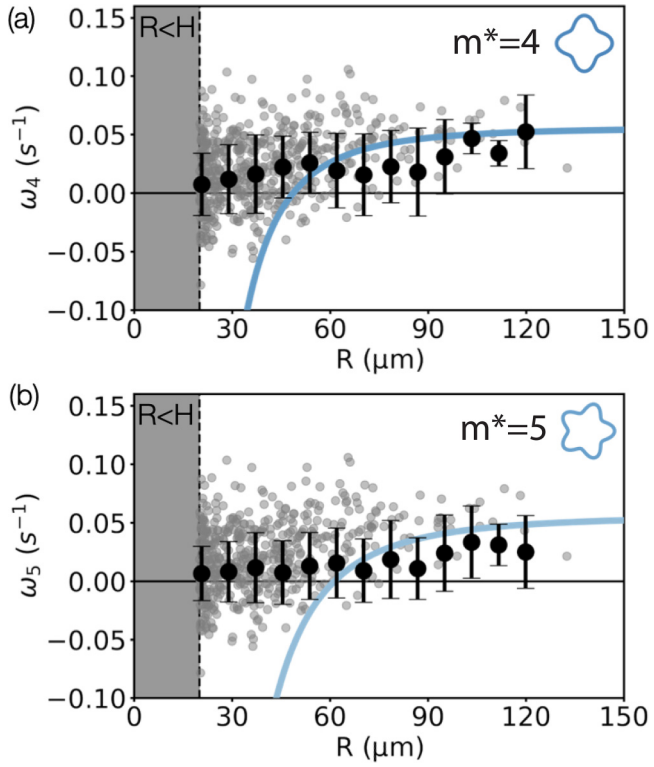


FIG. 16. Measured growth rates (gray dots) and model growth rates (blue curves) for the (a) fourth and (b) fifth radial harmonics. The model parameters are determined by fitting to only ω_2 in Fig. 2(a). For ω_4 and ω_5, the model prediction is obtained without adjusting these parameters. Error bars represent the standard deviation of the binned growth rates.

its subsequent relaxation. In practice, when our model predicts that a droplet's mode should have a large negative growth rate, we measure a growth rate near zero and see that the radial mode amplitudes are roughly constant over time. The initial amplitude of the initial perturbation is often smaller than our spatial resolution (~ 1 μm), so the amplitude appears constant. Moreover, the characteristic timescale for stable modes to relax is often smaller than our frame rate (0.2 frames/s), so we miss the exponential decay in the mode amplitude. The limitations in our measurements of negative growth rates can be seen in the growth rates of the fourth and fifth radial modes [Figs. 16(a) and 16(b)] since their critical radii are much larger. For example, the model predicts the critical radius of the fifth radial mode to be around 60 μm and that all droplets whose radii are below this should have large negative growth rates. However, we observe a distribution of growth rates mostly centered around zero in this region.

8. Stability of active droplets

As discussed in the main text, we do not measure a statistically significant radius below which active droplets are stable. Still, stable droplets do exist. We observe that the percentage of stable droplets mostly decreases as the droplet radius increases. The lack of a well-defined critical radius in experiments may be due to variability in the initial conditions between individual droplets—such as the microtubule network arrangement, protein concentration, or local heterogeneity in the surface treatment. We quantify the percentage of droplets that are stable for each mode as the ratio of the number of droplets which are stable $\omega_m < 0$ to the total number of droplets in that radius bin (Fig. 17). Generally, the percentage of stable droplets decreases with increasing radius. However, the percentage of stable droplets for $m = 2$ begins to increase at large radii. Our model predicts that at sufficiently large radii, ω_2 decays back to zero, but given the heterogeneity in the experimental data, when $\omega_2 \to 0^+$ the experimental droplets will have a distribution of growth rates centered around $\omega_2 = 0$. Assuming that the distributed growth rates are centered around zero with no skewness, we expect 50% of the droplets to be stable.

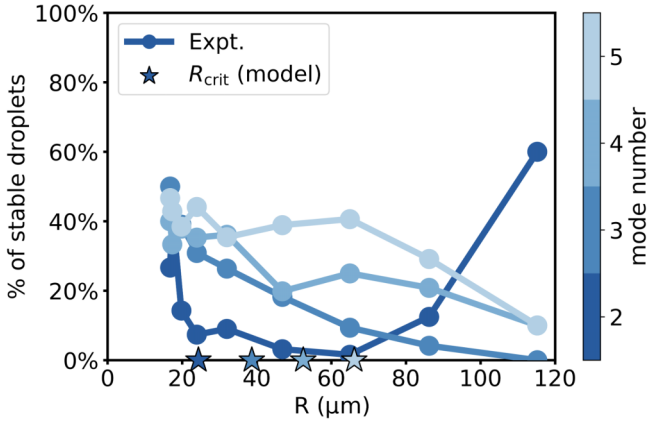


FIG. 17. Stability of experimental active droplets. Although our model predicts a critical radius above which all droplets are unstable, experimental active droplets are heterogeneous and exhibit a range over which droplets become unstable. The percentage of stable active droplets generally decreases as droplet radius increases. Each radial mode has a critical radius associated with it given by $\omega_m(R_{crit}) = 0$, shown as a star.

9. Droplet $m = 0$ growth rate

Mode 0 corresponds to a change in the droplet's cross-sectional area. While our model predicts zero growth of the zero mode number due to incompressibility, experiments measure nonzero growth of the zeroth radial harmonic. The growth rate of mode zero mostly decreases with droplet radius [Fig. 18(a)] and is an order of magnitude less than the growth rate of the unstable modes [Figs. 2(a) and 2(b)].

We hypothesize two possible origins of this in-plane area growth. First, active droplets have different wetting properties from passive droplets. Upon uncaging the ATP, the contact angle the droplet forms with the glass substrate may change, consequently changing the in plane area of the active fluid. Second, we observe the microtubule network dilates when the activity is turned on. Before the ATP is released, kinesin molecular motors crosslink the microtubule network and the system forms a solidlike gel. However, this solidlike gel does not fill the entire Dextran-rich droplet [Fig. 18(b)]. Upon releasing the ATP, the kinesin-microtubule network is fluidized and expands, thus filling the entire Dextran-rich droplet [Fig. 18(c)].

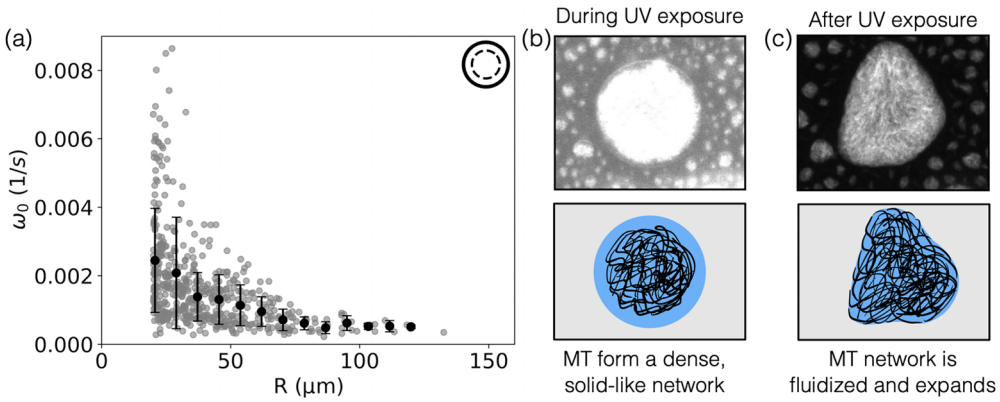


FIG. 18. Droplet dilational mode. (a) Growth rate of the zeroth radial harmonic is nonzero and largest for droplets whose radii is close to the gap height. (b), (c) One possible explanation for the nonzero growth rate of mode zero lies in that we are imaging the microtubule network and not the fluid interface itself. The network is initially dense and solidlike before the ATP is fully released. Once the ATP is released, the network is fluidized and expands.

10. Flat interface $q = 0$ growth rate

Initially flat active-passive interfaces also exhibit nonzero growth rate of the zero wave number mode, as shown in Figs. 19(a) and 19(b). The growth rate of the zero wave number mode is on the same order of magnitude as the unstable modes, unlike active droplets whose zero mode growth rate is one order of magnitude less than the unstable modes. The significant growth of the zero wave number at an initially flat interface may originate from the unique way we construct the interface which leads to density variations in the microtubule network, as detailed below.

11. Microtubule Density Heterogeneity

At the initially flat active/passive interface, we observe spatial heterogeneity in the microtubule intensity signal, which suggests spatial heterogeneity in the local microtubule density. We observe variations in the microtubule concentration parallel and perpendicular to the initially flat interface [Figs. 20(a) and 20(b)]. The compressibility of the microtubule network is not considered in our present model, which models the active nematic liquid crystal as incompressible, but it may drive the growth of the zero wave number mode in the flat interface.

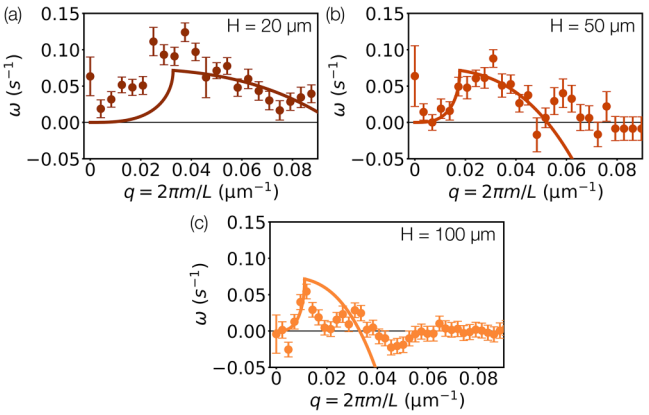


FIG. 19. Flat interface dilational mode. Flat interfaces have nonzero growth at zero wave number for (a) $H = 20\,\mu m$ and (b) $H = 50\,\mu m$ but not (c) $H = 100\,\mu m$. The growth rate of the zero wave number is on the same order of magnitude as the growth rates of the unstable wave numbers.

12. Anisotropy in the phases of the radial modes

Another discrepancy between the model and experimental measurements is in the phases (orientation) ϕ_m of the radial harmonics. While our model predicts the phases are unbiased and isotropic, experiments find slight anisotropy [Fig. 21(a)]. We quantify the strength of the anisotropy using the order parameter $\mathcal{Q}_m = \sqrt{\langle \cos \phi_m \rangle^2 + \langle \sin \phi_m \rangle^2}$. Mode 1 (translation)

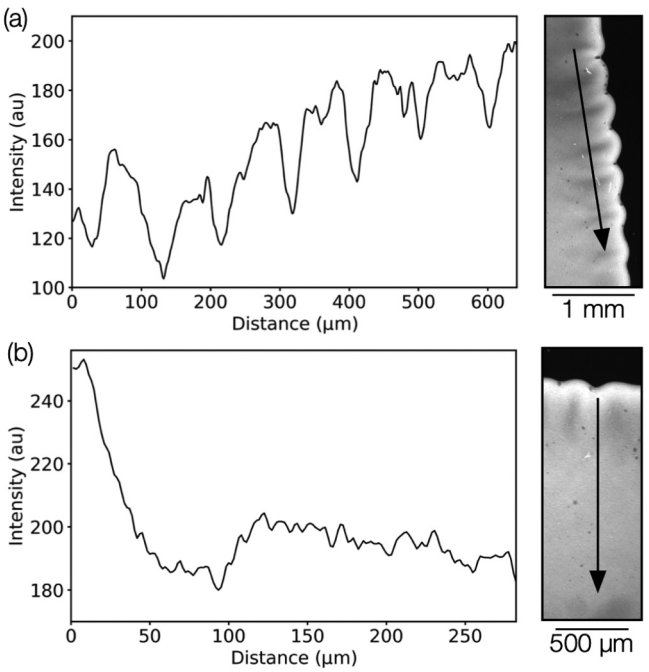


FIG. 20. Microtubule density variations. The fluorescent intensity of microtubules is proportional to the local microtubule concentration. We observe variations in fluorescence intensity, and hence microtubule density, (a) parallel and (b) perpendicular to the interface.

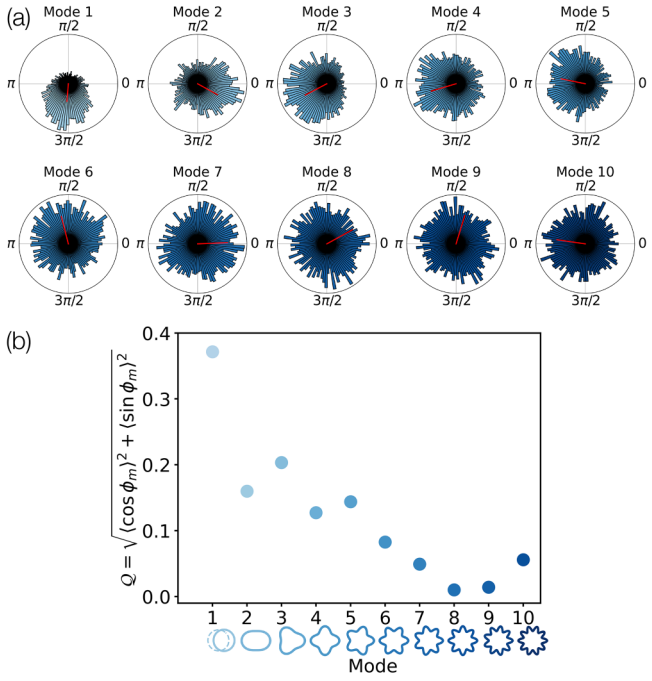


FIG. 21. Anisotropy of radial harmonics. (a) Histograms of the argument of the complex Fourier coefficients, $\phi_m = \arg a_m$. The red line is the average direction distribution. (b) The strength of the anisotropy is quantified using the order parameter $\mathcal{Q}_m = \sqrt{\langle\cos\phi_m\rangle^2 + \langle\sin\phi_m\rangle^2}$. Anisotropy largely decreases with mode number and is largest in mode 1 (translation).

has the largest anisotropy [Fig. 21(b)] and has the average orientation $\langle\phi_1\rangle \approx 3\pi/2$. Droplets are flowed in to the channel along the $\pi/2, 3\pi/2$ axis, which may cause the anisotropy in

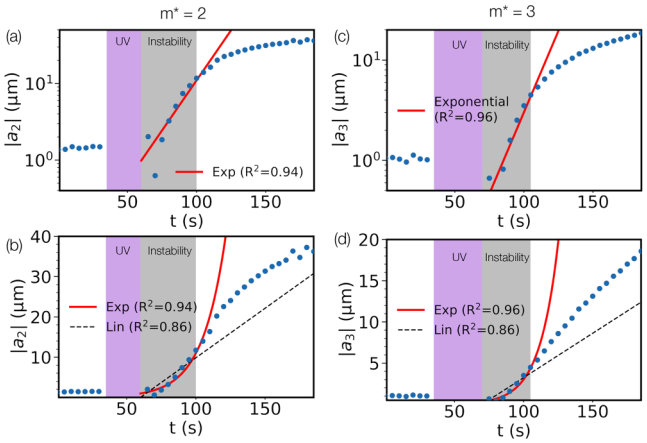


FIG. 22. Characteristic plots of the temporal evolution of the fastest-growing radial mode for droplets with (a), (b) $m^* = 2$ and (c), (d) $m^* = 3$ in $H = 50\,\mu$m gap height. The amplitude of the mode grows exponentially, shown in panels (a) and (c) log-lin and panels (b) and (d) lin-lin axes, after the ATP is released via UV exposure. The exponential fits have a larger R^2 value than the linear fits, but we note there is a limited time resolution of experimental data points during the linear instability.

mode 1 along the $3\pi/2$ direction. The anisotropy in modes 2+ may arise from the initial conditions of the microtubule network. When droplets are flowed into the Hele-Shaw cell, the microtubule network is initially passive and susceptible to shear-driven alignment. Any shear-imposed alignment of the microtubule network may bias the orientation of the unstable modes in the interfacial instability. Representative time traces and exponential fits used to measure growth rates are shown in Fig. 22.

[1] W. D. Smyth and J. N. Moum, Ocean mixing by Kelvin-Helmholtz instability, Oceanography **25**, 140 (2012).

[2] W. Moon, G. E. Manucharyan, and H. A. Dijkstra, Baroclinic instability and large-scale wave propagation in a planetary-scale atmosphere, Q. J. R. Meteorol. Soc. **148**, 809 (2022).

[3] P.-T. Brun, C. Inamura, D. Lizardo, G. Franchin, M. Stern, P. Houk, and N. Oxman, The molten glass sewing machine, Philos. Trans. R. Soc. A **375**, 20160156 (2017).

[4] H. Yuk and X. Zhao, A new 3D printing strategy by harnessing deformation, instability, and fracture of viscoelastic inks, Adv. Mater. **30**, 1704028 (2018).

[5] J. Bear, *Dynamics of Fluids in Porous Media* (Courier Corporation, Chelmsford, MA, 2013).

[6] Z. Yang, Y. Méheust, I. Neuweiler, R. Hu, A. Niemi, and Y.-F. Chen, Modeling immiscible two-phase flow in rough fractures from capillary to viscous fingering, Water Resour. Res. **55**, 2033 (2019).

[7] B. Gouveia, S. U. Setru, R. Alfaro-Aco, J. W. Shaevitz, H. A. Stone, and S. Petry, A hydrodynamic instability drives protein droplet formation on microtubules to nucleate branches, Biophys. J. **120**, 215A (2021).

[8] R. Bar-Ziv, T. Tlusty, E. Moses, S. A. Safran, and A. Bershadsky, Pearling in cells: A clue to understanding cell shape, Proc. Natl. Acad. Sci. USA **96**, 10140 (1999).

[9] M. Poujade, E. Grasland-Mongrain, A. Hertzog, J. Jouanneau, P. Chavrier, B. Ladoux, A. Buguin, and P. Silberzan, Collective migration of an epithelial monolayer in response to a model wound, Proc. Natl. Acad. Sci. USA **104**, 15988 (2007).

[10] E. Hannezo, J. Prost, and J.-F. Joanny, Mechanical instabilities of biological tubes, Phys. Rev. Lett. **109**, 018101 (2012).

[11] C. Pérez-González, R. Alert, C. Blanch-Mercader, M. Gómez-González, T. Kolodziej, E. Bazellieres, J. Casademunt, and X. Trepat, Active wetting of epithelial tissues, Nat. Phys. **15**, 79 (2019).

[12] R. Alert, C. Blanch-Mercader, and J. Casademunt, Active fingering instability in tissue spreading, Phys. Rev. Lett. **122**, 088104 (2019).

[13] J. O. Kessler, Hydrodynamic focusing of motile algal cells, Nature (London) **313**, 218 (1985).

[14] J. R. Platt, "Bioconvection patterns" in cultures of free-swimming organisms, Science **133**, 1766 (1961).

[15] N. Waisbord, C. T. Lefèvre, L. Bocquet, C. Ybert, and C. Cottin-Bizonne, Destabilization of a flow focused suspension of magnetotactic bacteria, Phys. Rev. Fluids **1**, 053203 (2016).

[16] I. Eisenmann, M. Vona, N. Desprat, T. Ishikawa, E. Lauga, and R. Jeanneret, Pure hydrodynamic instabilities in active jets of "puller" microalgae, Phys. Rev. Lett. **135**, 198301 (2025).

[17] A. Ganesh, C. Douarche, and H. Auradou, Active Saffman-Taylor viscous fingering, Phys. Rev. Lett. **134**, 128301 (2025).
[18] E. Ben-Jacob, From snowflake formation to growth of bacterial colonies, II: Cooperative formation of complex colonial patterns, Contemp. Phys. **38**, 205 (1997).
[19] J. Yan, C. Fei, S. Mao, A. Moreau, N. S. Wingreen, A. Košmrlj, H. A. Stone, and B. L. Bassler, Mechanical instability and interfacial energy drive biofilm morphogenesis, eLife **8**, e43920 (2019).
[20] A. Martínez-Calvo, T. Bhattacharjee, R. K. Bay, H. N. Luu, A. M. Hancock, N. S. Wingreen, and S. S. Datta, Morphological instability and roughening of growing 3D bacterial colonies, Proc. Natl. Acad. Sci. USA **119**, e2208019119 (2022).
[21] F. Gallaire and P.-T. Brun, Fluid dynamic instabilities: Theory and application to pattern forming in complex media, Philos. Trans. R. Soc. A **375**, 20160155 (2017).
[22] M. C. Marchetti, J. F. Joanny, S. Ramaswamy, T. B. Liverpool, J. Prost, M. Rao, and R. A. Simha, Hydrodynamics of soft active matter, Rev. Mod. Phys. **85**, 1143 (2013).
[23] S. Ramaswamy, Active fluids, Nat. Rev. Phys. **1**, 640 (2019).
[24] D. Dell'Arciprete, M. L. Blow, A. T. Brown, F. D. C. Farrell, J. S. Lintuvuori, A. F. McVey, D. Marenduzzo, and W. C. K. Poon, A growing bacterial colony in two dimensions as an active nematic, Nat. Commun. **9**, 4190 (2018).
[25] I. H. Riedel, K. Kruse, and J. Howard, A self-organized vortex array of hydrodynamically entrained sperm cells, Science **309**, 300 (2005).
[26] T. Sanchez, D. T. N. Chen, S. J. DeCamp, M. Heymann, and Z. Dogic, Spontaneous motion in hierarchically assembled active matter, Nature (London) **491**, 431 (2012).
[27] J. Dunkel, S. Heidenreich, K. Drescher, H. H. Wensink, M. Bär, and R. E. Goldstein, Fluid dynamics of bacterial turbulence, Phys. Rev. Lett. **110**, 228102 (2013).
[28] R. Adkins, I. Kolvin, Z. You, S. Witthaus, M. C. Marchetti, and Z. Dogic, Dynamics of active liquid interfaces, Science **377**, 768 (2022).
[29] L. Zhao, P. Gulati, F. Caballero, I. Kolvin, R. Adkins, M. C. Marchetti, and Z. Dogic, Asymmetric fluctuations and self-folding of active interfaces, Proc. Nat. Acad. Sci. USA **121**, e2410345121 (2024).
[30] J. Berezney, B. L. Goode, S. Fraden, and Z. Dogic, Extensile to contractile transition in active microtubule–actin composites generates layered asters with programmable lifetimes, Proc. Natl. Acad. Sci. USA **119**, e2115895119 (2022).
[31] T. E. Bate, M. E. Varney, E. H. Taylor, J. H. Dickie, C.-C. Chueh, M. M. Norton, and K.-T. Wu, Self-mixing in microtubule-kinesin active fluid from nonuniform to uniform distribution of activity, Nat. Commun. **13**, 6573 (2022).
[32] S. Alam, B. Najma, A. Singh, J. Laprade, G. Gajeshwar, H. G. Yevick, A. Baskaran, P. J. Foster, and G. Duclos, Active Fréedericksz transition in active nematic droplets, Phys. Rev. X **14**, 041002 (2024).
[33] B. Najma, S. Ghosh, C. Amey, P. J. Foster, M. F. Hagan, A. Baskaran, and G. Duclos, Arrested coalescence, aging, and stability of asters composed of microtubules and kinesin motors, Phys. Rev. Res. **7**, 013247 (2025).
[34] L. J. Ruske and J. M. Yeomans, Morphology of active deformable 3D droplets, Phys. Rev. X **11**, 021001 (2021).
[35] A. Sciortino, H. A. Faizi, D. A. Fedosov, L. Frechette, P. M. Vlahovska, G. Gompper, and A. R. Bausch, Active membrane deformations of a minimal synthetic cell, Nat. Phys. **21**, 799 (2025).
[36] G. Salbreux and F. Jülicher, Mechanics of active surfaces, Phys. Rev. E **96**, 032404 (2017).
[37] A. Nagilla, R. Prabhakar, and S. Jadhav, Linear stability of an active fluid interface, Phys. Fluids **30**, 022109 (2018).
[38] H. Soni, W. Luo, R. A. Pelcovits, and T. R. Powers, Stability of the interface of an isotropic active fluid, Soft Matter **15**, 6318 (2019).
[39] T. Dhar, M. J. Shelley, and D. Saintillan, Stability of co-annular active and passive confined fluids, Phys. Rev. Fluids **10**, 083103 (2025).
[40] M. L. Blow, S. P. Thampi, and J. M. Yeomans, Biphasic, lyotropic, active nematics, Phys. Rev. Lett. **113**, 248303 (2014).
[41] Y. N. Young, M. J. Shelley, and D. B. Stein, The many behaviors of deformable active droplets, Math. Biosci. Eng. **18**, 2849 (2021).
[42] R. Alert, Fingering instability of active nematic droplets, J. Phys. A: Math. Theor. **55**, 234009 (2022).
[43] P. Chandrakar, M. Varghese, S. Aghvami, A. Baskaran, Z. Dogic, and G. Duclos, Confinement controls the bend instability of three-dimensional active liquid crystals, Phys. Rev. Lett. **125**, 257801 (2020).
[44] L. Paterson, Radial fingering in a Hele Shaw cell, J. Fluid Mech. **113**, 513 (1981).
[45] B. Najma, M. Varghese, L. Tsidilkovski, L. Lemma, A. Baskaran, and G. Duclos, Competing instabilities reveal how to rationally design and control active crosslinked gels, Nat. Commun. **13**, 6465 (2022).
[46] See Supplemental Material at http://link.aps.org/supplemental/10.1103/ytwv-7swk for the movie descriptions.
[47] F. C. Keber, E. Loiseau, T. Sanchez, S. J. DeCamp, L. Giomi, M. J. Bowick, M. C. Marchetti, Z. Dogic, and A. R. Bausch, Topology and dynamics of active nematic vesicles, Science **345**, 1135 (2014).
[48] P. Guillamat, Ž. Kos, J. Hardoüin, J. Ignés-Mullol, M. Ravnik, and F. Sagués, Active nematic emulsions, Sci. Adv. **4**, eaao1470 (2018).
[49] Y. Hatwalne, S. Ramaswamy, M. Rao, and R. A. Simha, Rheology of active-particle suspensions, Phys. Rev. Lett. **92**, 118101 (2004).
[50] M. Varghese, A. Baskaran, M. F. Hagan, and A. Baskaran, Confinement-induced self-pumping in 3D active fluids, Phys. Rev. Lett. **125**, 268003 (2020).
[51] P. G. D. Gennes, Phenomenology of short-range-order effects in the isotropic phase of nematic materials, Phys. Lett. A **30**, 454 (1969).
[52] D. Bensimon, L. P. Kadanoff, S. Liang, B. I. Shraiman, and C. Tang, Viscous flows in two dimensions, Rev. Mod. Phys. **58**, 977 (1986).
[53] C. Joshi, S. Ray, L. M. Lemma, M. Varghese, G. Sharp, Z. Dogic, A. Baskaran, and M. F. Hagan, Data-driven discovery of active nematic hydrodynamics, Phys. Rev. Lett. **129**, 258001 (2022).
[54] D. A. Gagnon, C. Dessi, J. P. Berezney, R. Boros, D. T.-N. Chen, Z. Dogic, and D. L. Blair, Shear-induced gelation of self-yielding active networks, Phys. Rev. Lett. **125**, 178003 (2020).
[55] D. Marenduzzo, E. Orlandini, and J. M. Yeomans, Hydrodynamics and rheology of active liquid crystals: A numerical investigation, Phys. Rev. Lett. **98**, 118102 (2007).

[56] Complex growth rates imply the existence of traveling waves [38]. The study of these waves is out of the scope of this paper. Traveling waves have been observed in the nonlinear regime [28].

[57] K.-T. Wu, J. B. Hishamunda, D. T. N. Chen, S. J. DeCamp, Y.-W. Chang, A. Fernández-Nieves, S. Fraden, and Z. Dogic, Transition from turbulent to coherent flows in confined three-dimensional active fluids, Science **355**, eaal1979 (2017).

[58] H. Wioland, F. G. Woodhouse, J. Dunkel, J. O. Kessler, and R. E. Goldstein, Confinement stabilizes a bacterial suspension into a spiral vortex, Phys. Rev. Lett. **110**, 268102 (2013).

[59] Y.-C. Chen, B. Jolicoeur, C.-C. Chueh, and K.-T. Wu, Flow coupling between active and passive fluids across interfaces, Sci. Rep. **11**, 13965 (2021).

[60] P. G. de Gennes and J. Prost, *The Physics of Liquid Crystals*, 2nd ed. (Oxford University Press, Oxford, 1995).

[61] S. M. Troian, E. Herbolzheimer, and S. A. Safran, Model for the fingering instability of spreading surfactant drops, Phys. Rev. Lett. **65**, 333 (1990).

[62] P. Gulati, F. Caballero, I. Kolvin, Z. You, and M. C. Marchetti, Traveling waves at the surface of active liquid crystals, Soft Matter **20**, 7703 (2024).

[63] P. G. Saffman and G. I. Taylor, The penetration of a fluid into a porous medium or Hele-Shaw cell containing a more viscous liquid, Proc. R. Soc. London A **245**, 1242 (1958).

[64] A. W. C. Lau, A. Prasad, and Z. Dogic, Condensation of isolated semi-flexible filaments driven by depletion interactions, Europhys. Lett. **87**, 48006 (2009).